Journal of Environmental Chemical Engineering 13 (2025) 118472

Contents lists available at ScienceDirect

Journal of Environmental Chemical Engineering

journal homepage: www.elsevier.com/locate/jece

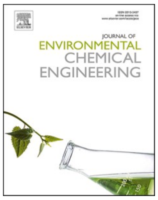

Optimisation of the quantum yield of carbon quantum dots prepared from bergamot pomace by means of a full factorial experimental design

Emanuele Zanda [a], Anna Irto [a], Salvatore Giovanni Michele Raccuia [a], Clemente Bretti [a], Giovanna De Luca [a], Ileana Ielo [a], Mariosimone Zoccali [b], Alessia Arena [c], Giuseppe Paladini [b], Francesco Caridi [b], Mauro Formica [d], Eleonora Macedi [d], Valentina Venuti [b], Concetta De Stefano [a], Luigi Mondello [a,e], Paola Cardiano [a,*], Gabriele Lando [a]

[a] *Dipartimento di Scienze Chimiche, Biologiche, Farmaceutiche ed Ambientali, Università degli Studi di Messina, Viale Ferdinando Stagno d'Alcontres, 31, Messina 98168, Italy*

[b] *Dipartimento di Scienze Matematiche e Informatiche, Scienze Fisiche e Scienze della Terra, Università degli Studi di Messina, Viale Ferdinando Stagno d'Alcontres, 31, Messina 98168, Italy*

[c] *Chromaleont s.r.l., c/o Dipartimento di Scienze Chimiche, Biologiche, Farmaceutiche ed Ambientali, Università degli Studi di Messina, former Veterinary School, Università degli Studi di Messina, Viale G. Palatucci snc, Messina 98168, Italy*

[d] *Dipartimento di Scienze Pure e Applicate, Università degli Studi di Urbino "Carlo Bo", Via della Stazione 4, Urbino 61029, Italy*

[e] *Messina Institute of Technology, c/o Dipartimento di Scienze Chimiche, Biologiche, Farmaceutiche ed Ambientali, Università degli Studi di Messina, Former Veterinary School, Università degli Studi di Messina, Viale G. Palatucci snc, Messina 98168, Italy*

ARTICLE INFO

Keywords:
Green synthesis
Hydrothermal treatment
Carbon nanomaterials
Biomass valorisation
Circular economy
Variables interaction
Response surface
Luminescence

ABSTRACT

Carbon Quantum Dots (CQDs) are versatile nanomaterials known for their tuneable optical properties and strong photoluminescence, making them suitable for potential use in various environmental and sensing applications. In this study, CQDs were synthesized *via* hydrothermal treatment of bergamot pomace, a citrus industry byproduct, in line with green chemistry and circular economy principles. A full factorial experimental design was employed to systematically optimize the quantum yield (Φ) by varying reaction time, temperature, and precursor concentration. The best model included positive linear parameters, interaction terms involving temperature and time, as well as the quadratic parameter for the precursor concentration. The quadratic parameters relative to time were found to be negative and indicated an optimised reaction time at $\sim$ 9 h. The resulting CQDs were extensively characterized. UV-Vis absorption and fluorescence spectroscopy showed the typical CQD optical features with minor variations depending on the synthesis conditions. Raman spectroscopy revealed characteristic D and G bands and allowed for an estimation of the particle diameters ($\leq$ 62.28 nm), while TEM measurements showed particle size up to 52.5 nm, with higher uniformity for lower reaction temperatures. DLS suggests the nanoparticle aggregation in aqueous solution, supported by HPLC which also revealed two distinct CQDs families. ATR-FTIR and potentiometric titrations indicate predominance of carboxylate groups on the product surface. Overall, this study presents a structured optimization strategy for enhancing CQD properties from renewable feedstocks and highlights their potential for future integration into environmental monitoring systems.

1. Introduction

Due to their highly tuneable luminescent and electrochemical properties, carbon and graphene quantum dots are central to current scientific inquiry into zero-dimensional nanomaterials, resulting in a highly active field of research [1–3]. The broad applicability of their luminescent and electrochemical properties has been fruitfully employed in optoelectronics, sensing, as well as energy-related or biological applications [4–7], solidifying their status as a rapidly evolving area of scientific investigation. Carbon Quantum Dots (CQDs) have

---

[*] Corresponding author.
E-mail address: paola.cardiano@unime.it (P. Cardiano).

https://doi.org/10.1016/j.jece.2025.118472
Received 12 June 2025; Received in revised form 30 July 2025; Accepted 3 August 2025

particle sizes typically smaller than 10 nm, a carbonaceous core consisting of sp^2- and sp^3-hybridised carbon atoms, and different functional groups on their surface that depend on the precursor material and synthesis procedure [8,9]. A rich tuneability of CQDs chemical and physical properties has been achieved by surface modification, such as covalent or supramolecular functionalisation [10–12], and by doping with various heteroatoms [13–17]

Following their accidental discovery by Xu *et al.* in 2004 [18], CQDs have gained significant attention for their advantageous properties, including strong fluorescence, water solubility, chemical stability, low toxicity, biocompatibility, and ease of surface modification [19]. Among these, their photoluminescence properties have been widely studied and extensively exploited, particularly in sensing applications [13,20–22].

CQDs frequently exhibit high selectivity and sensitivity towards diverse analytes, including metal ions, anions, biomolecules, water pollutants, and other chemicals. The predominant sensing mechanism involves fluorescence quenching (dynamic and static), with selectivity being significantly influenced by core structure, surface functionality, size, and morphology [23].

In metal ions (M^{n+}) sensing, fluorescence quenching typically arises from the interaction between M^{n+} and surface functional groups, forming metal complexes [9]. Surface doping with heteroatoms such as nitrogen, sulfur, or phosphorus can further enhance selectivity for specific M^{n+}. Indeed, a deep understanding of CQD surface chemistry is essential for refining and improving their sensing capabilities [24,25].

The broad array of precursors available for CQD synthesis is a key advantage. These include pure organic molecules such as carbohydrates [26], amino acids [27,28], and acids [29,30], alongside biomass-derived carbon sources [9,31–34]. Notably, the exploitation of waste and by-products from the food processing industry for CQD production aligns with the principles of Green Chemistry [35] and Circular Economy [36], highlighting the sustainability potential of this field.

Several synthetic strategies have been developed for CQDs using pure reagents and biomasses. Common methods include hydrothermal or solvothermal treatment, high-temperature pyrolysis, microwave irradiation, and electrochemical oxidation [37]. Hydrothermal treatment, involving heating a water suspension of the precursor under pressure at moderate temperatures [32], stands out as a widely adopted and environmentally benign method, consistent with Green Chemistry principles.

Synthesis parameters, such as reaction time, temperature, solvent type, and precursor quantity, vary significantly among the different studies. Their choice impacts particle size, surface functionalisation, and the resulting chemical and photoluminescence properties, including quantum yields (Φ). Reaction temperatures typically fall between 120 °C and 260 °C, while reaction times span a range of 2–36 h (h) [32]. Precursor quantities are often chosen arbitrarily, with reported values ranging from hundreds of milligrams to tens of grams in the literature.

For instance, Zhao *et al.* hydrothermally treated 50 g of corn dispersed in 20 cm^3 of water at 200 °C for 10 h, obtaining CQDs with a Φ of 14.9 % and a particle size of 3.5 nm after purification [38]. In contrast, Wu *et al.* used 1 g of dried corn cob dispersed in 30 cm^3 of water, synthesising CQDs at 180 °C for 12 h, yielding a smaller particle size of 2.5 nm but a significantly lower Φ of 1 % [39].

Optimising synthesis parameters to achieve high-Φ CQDs from biomass is challenging, mainly due to the interplay of multiple variables. Most reported syntheses rely on the one-variable-at-a-time approach [32], which does not account for the possible interactions between the parameters, thus limiting the control over the features of the resulting CQDs. Chemometric tools such as experimental design [40] can address this challenge, allowing for a systematic understanding of the synthesis process and optimisation of reaction conditions. However, only a few studies applied experimental design approaches to CQD synthesis and focused on secondary parameters such as pH, the addition of other reagents, or the use of different solvents [41–44]. Nonetheless, initial precursor concentration, reaction time, and temperature are predominantly present for the preparation of the carbon nanoparticles, depending on the synthesis strategies. To the best of the authors' knowledge, no previous studies employed a full factorial experimental design to systematically evaluate the combined influence of the mentioned fundamental parameters on the hydrothermal synthesis of biomass-based CQDs. Although the same parameters were optimised for pyrolysis as the synthesis strategy [45,46], this work aims to assess, for the first time, the importance of the combined influence for the synthesis of biomass-based CQDs using the green strategy of the hydrothermal synthesis.

In this context, our study focuses on using bergamot pomace (BP) as a precursor for the synthesis of CQDs. With approximately 90 % of global production concentrated in southern Italy [47,48], bergamot is a citrus fruit whose peel is a valuable source of essential oils in the pharmaceutical, cosmetic, and food industries. A significant challenge is posed by the 50–60 % of waste generated during extraction, necessitating the development of sustainable disposal strategies [47].

The use of bergamot pomace, which has previously shown a good affinity for Cd^{2+} ions [49], can be a sustainable approach for producing CQDs as a convenient upcycling strategy aimed at developing new biocompatible materials with potential applications in metal ion sensing, biosensing, and catalysis. A full factorial experimental design was employed to optimise the green hydrothermal synthesis of CQDs from lyophilised bergamot pomace. This chemometric strategy enabled the identification of optimal synthesis conditions to maximise Φ, the key variables to be optimised being reaction time and temperature, as well as the initial amount of bergamot pomace.

Representative samples from the various syntheses were characterised using multiple techniques to evaluate their properties. Absorption and emission spectroscopy were used to assess the effective formation of CQDs based on their optical features. Surface Enhanced Raman Scattering (SERS) measurements confirmed the presence of a graphitic nanoparticle core and provided a particle size estimation consistent with Transmission Electron Microscopy (TEM) observations. Dynamic Light Scattering (DLS) revealed the ζ-potential and hydrodynamic diameter of CQDs, suggesting aggregation in aqueous solution. This observation was supported while further purification was attempted through High Performance Liquid Chromatography (HPLC). This separation technique allowed for the identification of two distinct CQD families and the determination of the corresponding Φ.

Finally, Attenuated Total Reflectance in Fourier Transform Infrared (ATR-FTIR) spectroscopy was used for structural characterisation, revealing the presence of oxygen-containing surface functional groups whose acid-base behaviour was evaluated by potentiometric titrations.

2. Materials and methods

2.1. Reagents

Bergamot pomace (BP), sourced from Capua 1880 company (Reggio Calabria, Italy), was collected from the *Femminello* and *Fantastico* cultivars between November 2021 and January 2022. The biomass, comprising seeds, pulp, and deoiled citrus flavedo after juice and essential oil extraction, was lyophilised for around 72 h at T = -50 °C under vacuum, using a LyoQuest-55 freeze dryer (Telstar, Spain). The lyophilised residue was then ground using a coffee grinder (Moulinex, Group SEB, France).

Hydrochloric acid and sodium hydroxide solutions were prepared from the dilution of concentrated Titrisol ampoules (Merck, Milan, Italy, purity ≥ 99 %) and standardised against sodium carbonate and potassium hydrogen phthalate, respectively, both purchased from Fluka company (Darmstadt, Germany) with purity ≥ 99 %, after drying at $T = 110$ °C for 2 h. The ionic medium solutions preparation was performed by weighing the corresponding NaCl solid salt (Sigma-Aldrich, Milan, Italy, purity ≥ 99.0 %), previously dried at $T = 110$ °C for 2 h as well.

Quinine hemisulfate salt monohydrate (BioReagent, ≥ 99.0 %) was purchased from Merck (Darmstadt, Germany), and sulfuric acid (H_2SO_4, 95–97 %) was purchased from Sigma Aldrich (Milan, Italy).

Silver(I) acetylacetonate (Ag(acac)), sodium chloride (NaCl), acetone, and ultrapure water (UPW) for silver nanoparticle preparation were purchased from VWR (Milan, Italy). Ammonium hydroxide (NH_4OH) and hydrogen peroxide (H_2O_2) were supplied from Merck (Milan, Italy). Si wafers were purchased from Siegert Wafer (Aachen, Germany).

For the CQDs purification by HPLC, methanol (MeOH, grade 99.9 %) and water were supplied from Merck Life Science (Merck KGaA, Darmstadt, Germany).

2.2. CQDs preparation and purification

Aliquots of lyophilised BP (200, 250, 300 or 450 mg) were transferred into a 50 cm^3 DONLAB Teflon-lined stainless-steel autoclave (LabWare, Germany) and dispersed in 25 cm^3 of deionised water. The autoclave was then heated in a Digitheat oven (JP Selecta, Spain) at the desired temperature (150, 180 or 210 °C) and for a specific time (3, 6, 9, 15, or 18 h). After heating, the reactor was allowed to cool naturally to room temperature. The resulting solution and biochar were then dialysed in a dialysis bag (Cellu Sep H1, retaining molecular weight: 1000 Da) submerged in 1 dm^3 deionised water for 48 h. During this time, the water was changed thrice.

Following the dialysis, the solution was centrifuged using a Neya 16 R (XS instrumentations, Italy) centrifuge and filtered through a 0.22 µm-pore cellulose acetate membrane (Branchia, Spain). The obtained CQDs solution was finally dried at 65 °C under a vacuum using a Heidolph Laborota 4001 (Deltek srl, Italy) rotavapor coupled with a water-cooling system (ThermoScientific, Germany) and a membrane vacuum pump (Vacuumbrand, Germany). The obtained dried product was redissolved in deionised water for further studies.

2.3. Spectrophotometric measurements and quantum yield evaluation

Quantum Yield (Φ), corresponding to the ratio between emitted and absorbed photons, was calculated using quinine sulfate in 0.05 mol dm^{-3} H_2SO_4 as a reference according to Eq. 1 [50].

$$\Phi_s = \Phi_r \times \frac{F_s}{F_r} \times \frac{1-10^{A_r}}{1-10^{A_s}} \times \left(\frac{\eta_s}{\eta_r}\right)^2 \tag{1}$$

In this equation, F is the area of the emission spectrum ($\lambda_{ex} = 355$ nm; slit width is 2 nm); A is the absorbance at the excitation wavelengths (355 nm), and η is the refractive index of the solvent; s and r indexes indicate the sample (CQDs) and the reference (quinine sulfate), respectively. Since water was used as a solvent for both sample and reference, the refractive index term equals 1.

Quantum yield was assessed for each sample using three independent solutions at three different concentrations.

UV–visible absorption spectrophotometric studies were conducted using an Evolution 220 Thermo Scientific UV–visible spectrophotometer. Spectrofluorimetric experiments were performed using a FluoroMax-4 Horiba (Santa Barbara, United States) Jobin-Yvon spectrofluorometer. Quartz cells (Hellma Analytics) with a path length of 10 mm were used for all measurements.

2.4. Full factorial experimental design

The measured quantum yield of CQD samples prepared from lyophilised BP was optimised by means of a full factorial experimental design [40]. The investigated factors were the initial amount of BP (w), the reaction time (t), and the reaction temperature (T).

Initially, a 2^3 design with two levels for each factor was explored, namely a high level (+1) with $w = 300$ mg, $t = 9$ h, and $T = 210$ °C, and a low level (–1), with $w = 200$ mg, $t = 3$ h, and $T = 150$ °C. A central experimental point (0) corresponding to $w = 250$ mg of BP, $t = 6$ h, and $T = 180$ °C was also added and used to validate the model.

BP mass levels were chosen arbitrarily due to variability in the literature regarding biomass amount for CQDs synthesis; t was chosen considering 9 h to be a reasonable amount of time for the reaction being an intermediate value between the several studies on hydrothermal synthesis of biomass-based CQDs [32]; T was selected based on the working range of the reactor, whose highest limit is 210 °C. Experiments were performed in a random order to verify the reproducibility of the model and validate it. The syntheses at the central point and in another condition were performed in triplicate.

The model was computed as multilinear regression (MLR) according to Eq. 2 (initially excluding the quadratic term) using the CAT (Chemometrics Agile Tool) software [51] employing the leave-one-out method. Different models were tested while considering the contribution of only the linear coefficients (b_i) and the inclusion of one or more interaction parameters (b_{ij}), either individually or simultaneously.

$$y = b_0 + \sum_{i=1}^{3} b_i x_i + \sum_{j\neq i=1}^{3} b_{ij} x_i \bullet x_j + \sum_{i=1}^{3} b_{ii} x_i^2 \tag{2}$$

Once the linear model was established and validated, additional experiments were carried out at different levels to evaluate the contribution of the quadratic parameters b_{ii}. The final matrix is reported in Table 1.

The response at the central point was not considered in the fitting processes and used only to validate the model after a t-test between the response predicted by the model and the experimentally determined one (variance σ was estimated as a pooled variance according to Eq. 3).

$$\sigma = \frac{\sum \Phi_i - \overline{\Phi}}{n-1} \tag{3}$$

2.5. Surface-enhanced raman scattering (SERS) measurements

Flat silicon substrates were initially cleaned by keeping the chips in an 80 °C-heated alkaline piranha solution (UPW, 30 wt% H_2O_2, and 28 wt% NH_4OH in a 5: 1: 1 vol ratio) for 20 min, followed by three thorough washings with generous amounts of UPW [52].

Silver nanoparticles (AgNPs) were synthesised through a slightly modified protocol by Giuffrida *et al.* [53,54]. Specifically, solid Ag(acac) was added to UPW in a thoroughly cleaned Erlenmeyer flask (final Ag^+ concentration: 1 mmol dm^{-3}), and the solution was kept under stirring (300 rpm) for 30 min at 25 °C. The formation of AgNPs was pointed out by the initially colourless liquid turning pale yellow in about 10 min. Solid NaCl was then added to the suspension (final concentration:

Table 1
Experimental matrix with the three factors and the corresponding levels.

Experiment	w (mg)	t (h)	T (°C)	w	t	T
1	200	3	150	–1	–1	–1
2	200	9	150	–1	+ 1	–1
3	200	3	210	–1	–1	+ 1
4	200	9	210	–1	+ 1	+ 1
5	200	9	210	–1	+ 1	+ 1
6	200	9	210	–1	+ 1	+ 1
7	300	3	150	+ 1	–1	–1
8	300	9	150	+ 1	+ 1	–1
9	300	3	210	+ 1	–1	+ 1
10	300	9	210	+ 1	+ 1	+ 1
11	250	6	180	0	0	0
12	250	6	180	0	0	0
13	250	6	180	0	0	0
14	250	9	180	0	+ 1	0
15	300	9	180	+ 1	+ 1	0
16	200	18	210	–1	+ 4	+ 1
17	450	15	210	+ 4	+ 3	+ 1

0.02 mol dm^{-3}), keeping the stirring active for 30 min. Finally, the colloid was left undisturbed for 24 h before use.

Surface-Enhanced Raman Scattering (SERS)-active substrates were prepared by (i) drop casting 0.02 cm^3 of the colloid onto freshly cleaned silicon substrates (0.5 × 0.5 mm^2), (ii) waiting 2 h for the samples to dry, and (iii-iv) repeating the first two steps once.

CQDs were deposited onto the above-described SERS-active substrates by drop casting 0.035 cm^3 of nanoparticle solution and waiting for the solvent to evaporate.

μ-Raman measurements were carried out on three different CQD samples deposited onto the prepared SERS-active substrates through a portable Raman "BTR 111 Mini-Ram TM" (B&W Tek, Inc., Newark, NJ, USA) spectrometer. The instrument operates with a 785 nm diode laser source and a thermoelectrically cooled CCD detector, with a 280 mW maximum laser power at the excitation port. SERS spectra were registered in the range 500 −2000 cm^{-1} with a resolution of 8 cm^{-1} and an acquisition time of 30 s × 10 scans. Instrument calibration was accomplished through the employment of a silicon chip peak falling at 520.6 cm^{-1}, ensuring optimal instrument performance. The system was coupled with a BAC151B Raman microscope with an 80 × objective, which guarantees a working distance of 1.25 mm and a laser beam spot size of 25 μm. The laser maximum power delivered to the samples was ~ 30 mW. Data elaboration, including baseline correction and a smoothing process, was achieved through the BWSpec 3.27 software. As far as the quantitative analysis of the 1300 cm^{-1}–1650 cm^{-1} range is concerned, a curve-fitting approach employing Voigt functions was applied to the experimental profiles by means of the PeakFit 4.0 software package. Features such as centre frequency, linewidth, and intensity were kept free to change upon iterations. The goodness of the "best-fit" profiles was attested by an $r^2 \sim 0.9988$ for all the analysed spectra.

2.6. Transmission electron microscopy (TEM) measurements

The CQD samples were adsorbed for 24 h on gold grids for Transmission Electron Microscopy (grid size 300 mesh x 83 μm pitch). The grids were then analyzed by a Hitachi Transmission Electron Microscope HT7800 equipped with a LaB_6 electron gun and operating with an accelerating voltage of 20–120 kV. The images acquired for each sample were elaborated with the ImageJ software for the evaluation of the mean particle size (30 reads).

2.7. Light scattering measurements

Mean particle size and ζ-potential of CQDs were measured in solution at 25 °C by Dynamic and Electrophoretic Light Scattering using a Zetasizer Nano ZS instrument (Malvern Panalytical, Malvern, United Kingdom) equipped with a helium-neon 4 mW laser ($\lambda = 632.8$ nm) and at a scattering angle of 173°. The values for the Z average size and polydispersity index (*PdI*) of the CQDs were derived from a cumulants analysis of the experimental correlation curves, assuming a single particle size and applying a single exponential fit to the autocorrelation function [55]. The diameter and ζ-potential are then reported as a mean over three measurements, and the indicated uncertainty is the average absolute deviation. The measurements were performed using a folded capillary cell Zetasizer Nanoseries (Malvern, UK). In case of samples containing acetone, Quartz cells (Hellma Analytics) with a path length of 10 mm were employed. In the case of sonicated samples, an LBX Instruments ultrasound bath mod. ULTR (capacity 3.2 L; ultrasound frequency: 40 Hz, ultrasound power: 120 W; sonication time: 10 min) was used.

2.8. High performance liquid chromatography (HPLC) purification

The CQDs purification by HPLC was performed on a Shimadzu Prominence LC-20A system (Kyoto, Japan) equipped with: a CBM-20A communication bus module, a DGU-20A on-line degasser, two LC-20AD dual-plunger parallel-flow pumps, a SIL-20AC autosampler, a CTO-20A column oven, a SPD-M30A photodiode array detector, and a RF-20A$_{XS}$ fluorescence detector with a xenon lamp and wavelength range of 200–750 nm.

The analyses were carried out working in normal-phase mode using a silica column (15 cm × 3 mm × 5 μm d_p and a pore size of 90 Å Ascentis® Express 90 Å HILIC, Merck). The column oven temperature was 30 °C. The elution was performed as follows: 100 % MeOH (2 min) with a gradient of H_2O up to 100 % in 30 min. The flow rate was set to 0.4 cm^3 min^{-1}, and the injected volume was 0.03 cm^3. Data acquisition was performed by the LabSolutions Ver. 5.127 software (Shimadzu).

2.9. IR spectroscopy measurements

Attenuated Total Reflectance (ATR) in Fourier Transform (FT) Infrared (IR) spectroscopy was used to characterise the surface functional groups of 13 samples of CQDs using a Nicolet Thermo Scientific FT-IR spectrometer (iS50 model, Waltham, Massachusetts, United States of America) equipped with an ATR diamond window module. For each sample, 128 scans were accumulated with a spectral resolution of 4 cm^{-1} in the wavelength range between 4000 and 400 cm^{-1}.

Samples were prepared by diluting solid CQDs in 0.02 cm^3 of deionised water to obtain a highly concentrated solution, which was then deposited onto an aluminium foil [56] and left to dry at 60 °C to form a thin film. The blank was collected by contacting the aluminium foil with the ATR diamond, while sample spectra were registered by contacting the CQDs film with the ATR diamond.

2.10. Potentiometric titrations

The CQDs acid-base behaviour was investigated by means of potentiometric measurements carried out using a Metrohm 809 Titrando, equipped with an automatic burette ($V_{tot} = 10$ cm^3) and a combined glass microelectrode (6.0234.100 model), purchased from the Metrohm (Herisau, Switzerland) company. Titrant delivery, data acquisition, and electromotive force (potential, *e.m.f.*) stability were managed with the Metrohm TiAMO 2.5 software. Experiments were carried out in thermostated cells at $T = 25.0 \pm 0.1$ °C with a water-cooling system (ThermoScientific, Germany). The measurement solutions were constantly homogenised under stirring and flushed with pre-saturated $N_{2(g)}$ to remove and forestall the presence of $CO_{2(g)}$ and $O_{2(g)}$ inside. Variable amounts (0.30–0.85 mg) of the obtained CQDs dried samples were dissolved in 0.55–1.05 cm^3 deionised water to prepare different stock solutions, subsequently employed for the potentiometric experiments. 5 cm^3 of measurement samples were prepared by mixing variable volumes (0.45–0.90 cm^3) of stock solutions, hydrochloric acid ($c_{HCl} = 12.00$ mmol dm^{-3}) to regulate the starting pH ($pH_i \sim 2.0$), sodium chloride to fix ionic strength (*i.e.*, $I = 0.10$ mol dm^{-3}), and deionised water. Standard carbonate-free sodium hydroxide ($c_{NaOH} = 0.1016$ mol dm^{-3}) was employed to titrate the analysed solutions up to pH ~ 11.0. Before each experiment, the combined glass microelectrode was calibrated by carrying out titrations of HCl solutions at analogous pH_i and I/mol dm^{-3} conditions of the measurements, as well as the same titrant, providing the calculation of E^0 (standard electrode potential) and $\log K_w$ (water ionic product) values. Using the Nernst equation, the measured *e.m.f.* conversion into pH on a free scale (*i.e.*, pH = -log[H^+]) was performed.

The BSTAC computer program [57] was used for the refinement of the acid–base titrations parameters (E^0, $\log K_w$, acidic junction potential j_a, reagents analytical concentrations) and the determination of the CQDs acidic (protonation) constants. Their behaviour in aqueous solution was described by Eq. 4:

$$H^+ + X^- \rightleftharpoons HX \tag{4}$$

where X^- is an arbitrarily indicated mono-negatively charged active site exhibiting acid-base properties.

3. Results and discussion

3.1. Synthesis and purification of CQDs

BP, constituted by pulp, seeds, and peel, was freeze-dried, yielding a pale-yellow residue (Fig. S1(a)) that was ground into a fine and homogeneous powder to facilitate contact between BP and water and enhance reactivity. Hydrothermal treatment of this powder produced a yellow-orange solution with a short blue light luminescence under UV light and a solid black residue known as biochar (Fig. S1(b)).

In this study, the quantum yield (Φ) of CQDs prepared from bergamot pomace (BP) was optimised through a full factorial experimental design [40]. Table 2 presents the experimental matrix and the corresponding measured Φ values. For each experiment, Φ was measured three times using different aliquots of the same batch to assess the intrabatch variability. To evaluate the batch-to-batch reproducibility, three independent CQD batches were synthesised under identical conditions (*e.g.*, in experiments 4, 5, 6 and 11, 12, 13), and Φ was measured three times from different aliquots from each of these batches. The latter variability was not significantly different than the former ($F_{8,2} = 19.37$, $p > 0.05$).

Results indicated that temperature and reaction time significantly impacted the Φ of the products. This indication was also visually evident from the colour of the dialysed solution, which varied with T. When the synthesis was performed at 150 °C, the solutions were dark yellow-orange, while those obtained at 210 °C were pale yellow (Fig. S1(c)). Additionally, at 150 °C, the resulting biochar was brown rather than black, suggesting incomplete carbonisation. This observation aligned with the lowest Φ values in the experimental domain.

Table 2
Experimental matrix for the 2^3 full factorial design with the three factors, the corresponding levels, and experimentally determined Φ values.

Experiment	w (mg)	t (h)	T (°C)	w	t	T	Φ (%)
1	200	3	150	−1	−1	−1	0.65 0.64 0.64
2	200	9	150	−1	+ 1	−1	0.44 0.45 0.44
3	200	3	210	−1	−1	+ 1	0.78 0.83 0.86
4	200	9	210	−1	+ 1	+ 1	1.34 1.33 1.30
5	200	9	210	−1	+ 1	+ 1	1.64 1.47 1.52
6	200	9	210	−1	+ 1	+ 1	1.56 1.45 1.46
7	300	3	150	+ 1	−1	−1	0.61 0.64 0.63
8	300	9	150	+ 1	+ 1	−1	0.51 0.55 0.54
9	300	3	210	+ 1	−1	+ 1	1.02 1.07 1.06
10	300	9	210	+ 1	+ 1	+ 1	1.67 1.81 1.81
11	250	6	180	0	0	0	0.72 0.76 0.76
12	250	6	180	0	0	0	0.76 0.78 0.77
13	250	6	180	0	0	0	0.78 0.90 0.93

Experiments conducted in triplicate at the central point (experiments 11–13) and using 200 mg of BP heated at 210 °C for 9 h (experiments 4–6) yielded average Φ values of (0.80 ± 0.07) % and (1.5 ± 0.1) %, respectively. The low variability among the triplicates indicated that the synthesis procedure was reproducible.

To the best of our knowledge, only one other study reported a CQD synthesis from bergamot. In that study, 500 mg of bergamot was suspended in 10 cm^3 of water and heated in a 15 cm^3 autoclave at 200 °C for 5 h. Purification was only performed through filtration, leading to a product with a Φ of 50.78 %. The reported value is much higher than what was observed in this study. However, the pretreatment details for the raw material were not clearly described [58].

Other studies reported the hydrothermal synthesis of CQDs from citrus fruit biomasses without the addition of any other reagent. Hydrothermal synthesis at 180 °C from aqueous extract of *citrus clementine* peels yielded CQDs with $\Phi = 1.53$ %, comparable to this study [59].

A slightly higher value (4.29 %) was obtained from the hydrothermal treatment of dried orange peels at 200 °C and 8 h reaction time, while it was much higher for CQDs prepared from dried lemon seeds treated at 200 °C for 6 h ($\Phi = 13.3$ %) [60]. Treatment of pulverised *Citrus aurantium* at 130 °C and 9 h reaction time resulted in CQDs with $\Phi = 13.30$ % [61], while juice treated at 180 °C for 7 h yielded CQDs with Φ of 19.90 % [62]. The differences may reflect the different precursors, pre- and post-treatments of precursors and products, respectively, and the harvesting location and time of the biomasses, which influence their elemental composition [63]. For example, the presence of nitrogen resulted in higher CQD Φ, which is often exploited as a photoluminescence-enhancing strategy [15].

The experimental data in Table 2 were fitted to Eq. 2, initially considering the known term and the linear coefficients (b_i) and, subsequently, including one or more interaction parameters (b_{ij}) either individually or simultaneously taken. In the equation, x_1, x_2 and x_3 corresponded to the initial amount of BP (w), reaction time (t), and temperature (T), respectively.

For the evaluation of various models obtained by fitting experimental data to equations that considered the presence of different parameters, statistical parameters such as Explained Variance in Cross Validation (ECV, Eq. 5), the Root Mean Square Error in Cross Validation (RMSECV, Eq. 6) and b_0 values (Φ at the centre point) were computed and collected in Table S1.

$$\mathrm{ECV} = 100 - \frac{\sum_{\mathrm{i}=1}^{\mathrm{n}} \left(\Phi_{\mathrm{i}} - \widehat{\Phi}_{\mathrm{CV,i}}\right)^2}{\sum_{\mathrm{i}=1}^{\mathrm{n}} \left(\Phi_{\mathrm{i}} - \overline{\Phi_{\mathrm{i}}}\right)^2} \mathrm{ECV} \tag{5}$$

$$\mathrm{RMSECV} = \sqrt{\frac{\sum_{\mathrm{i}=1}^{\mathrm{n}} \left(\Phi_{\mathrm{i}} - \widehat{\Phi}_{\mathrm{CV,i}}\right)^2}{\mathrm{n}}} \mathrm{RMSECV} \tag{6}$$

In the equations, Φ_{i} are the experimentally measured quantum yields, $\widehat{\Phi}_{\mathrm{CV,i}}$ are those predicted during the cross-validation step, n is the number of experiments.

In addition to these parameters, the software provides the coefficient values along with their significance. The latter was evaluated based on the p-values: coefficients with $p < 0.001$ were considered highly significant; coefficients with $p > 0.01$ were considered not significant.

Results indicated that model 1 (see Table S1), which only accounts for the linear b_i coefficients, was not sufficient to describe the experimental data, showing an ECV of only 72.67 % and an RMSECV of 0.2414. Introducing the interaction coefficient b_{23}, which corresponds to the combined effect of t and T, a significant improvement in the fitting was evidenced, as ECV increased to values higher than 94 % and RMSECV decreased to values lower than 0.11. This evidence revealed that *w* had the least influence on the final *Φ* in the experimental domain.

Model 8 features the highest ECV (97.39 %) and the lowest RMSECV (0.07452). However, as evidenced in Table S2, the parameter b_{12} has no significance. Thus, model 7, which does not account for that parameter, was chosen as the one better describing the system. It presents an ECV value of 97.10 % and RMSECV of 0.07857, all parameters being highly significant. The obtained coefficients, along with their confidence intervals and significances, are listed in Table 3.

The results confirmed that the coefficient b_3, corresponding to *T*, had the greatest influence on the system, followed by *t* and *w*, as also evidenced by the response surfaces displayed in Fig. 1. The most important variations in *Φ* were observed as a function of *T*, followed by *t*.

The *Φ* values predicted by model 7 are in good agreement with the experimental data, as shown in Fig. 2. However, larger differences were observed for the experiments with higher *Φ* values, especially among experiments 4–6.

Given that a 2^3 full factorial design only allowed for the fitting of linear and interaction terms, additional experiments were conducted to gain more insights into the system, both within (experiments 14 and 15) and beyond (experiments 16 and 17) the experimental domain. The latter two experiments explored higher levels for *w* and *t*. Although *T* was the factor with the highest influence, further increases in its value were precluded by the operational limits of the reactor. The new experiments are listed in Table 4.

Experimental results revealed that, while keeping *T* fixed at 180 °C and *t* at 9 h (experiments 14 and 15), an increase in *w* resulted in a slight improvement of *Φ*. When *t* was extended to 18 h (level +4) with $w = 200$ mg (experiment 16), the resulting *Φ* values were similar to those achieved in experiments where all factors were set to level + 1 (experiment 10). A significant increase of *Φ* was observed when both *w* and *t* were increased outside the initial experimental domain (experiment 17). *Φ* reached the highest value (3.4 ± 0.3 %) when hydrothermally treating 450 mg of *BP* at 210 °C for 15 h. Although the observed values are quite low, they are still comparable to reported values for biomass-based CQDs obtained through the hydrothermal method [32].

The experimental data from experiments 1–10 and 14–17 were fitted altogether using different models based on Eq. 2, and the results are presented in Table S3.

The inclusion of the four experiments listed in Table 4 enhanced the capability to describe the system for the only linear terms b_i, increasing the ECV of model 1.2–80.53 % compared to 72.67 % for model 1. On the contrary, the previous best-fitting model (model 8), which included both linear and interaction terms, showed a reduced ECV from 97.39 % to 95.46 % in model 23. This effect was even more pronounced when moving from the previously selected model 7 to model 13, as the ECV decreased from 97.10 % to 91.19 %. The fittings with linear coefficients and only one quadratic term were among the models with the lowest ECV, with the exception of model 7.2. The best models, with ECV > 96 %, had in common the inclusion of the parameters b_{22} and b_{23}, highlighting the importance of reaction time to the final *Φ* of the product. The best fitting model for the extended experimental domain was model 58, which included all linear, interaction, and quadratic parameters, with the exception of the quadratic temperature coefficient b_{33}. This may reflect the limited exploration of *T*. Model 58 was characterised by the highest ECV of 97.47 % and the lowest RMSECV of 0.1183. The inclusion of b_{33} only (model 63) slightly decreased ECV to 97.36 % and increased RMSECV to 0.1209. However, as highlighted in Table S4, which report the coefficients, their confidence interval, and their significance, the parameter b_{12} has again no significance, and model 53, without that coefficient, was selected as the one better describing the system. The coefficients and selected parameters are reported in Table 5.

Table 3
Coefficients obtained from the fitting of model 7, their confidence interval and significance.

Coefficient	Value	Confidence interval	*p*-value
b_0	0.91	0.03	< 0.001
b_1	0.08	0.03	< 0.001
b_2	0.13	0.03	< 0.001
b_3	0.35	0.03	< 0.001
b_{13}	0.06	0.03	< 0.001
b_{23}	0.20	0.03	< 0.001

As previously observed, all linear and interaction coefficients considered were positive, with the highest value being b_3, followed by b_{23}, highlighting the importance of the temperature in the synthesis of CQDs. The coefficients taking *w* into account, *i.e.*, b_1 and b_{13}, had the lowest values.

The quadratic coefficient b_{11} was also positive, whereas b_{22} was negative and had a higher significance. This behaviour could be visually observed from the response surfaces: Fig. 3(a) presents a maximum for a reaction time of ~ 9 h (level +1), consistently observing a linear increase of *Φ* as a function of *T*, while a non-linear increase of *Φ* as a function of *w* appeared at both low and high *T* (Fig. 3(b) and (c)). Fig. 3 (c) highlights how raising *t* at low *T* led to a decrease in *Φ*, while *Φ* increased on increasing *t* at high *T*.

The tool of the experimental design was already exploited in order to optimise the *Φ* of CQDs. However, other parameters and experimental strategies were explored, such as the addition of other reagents as nitrogen sources [41,42], acid [43], or solvents [44]. Ma *et al.* optimised the reaction temperature, time, and quantity of peanut shells using pyrolysis as a thermal treatment. They observed significant influences from the linear coefficients of *T* and *w*, as well as from the interaction between *T* and *t*, all of which were positive. Quadratic terms for *T* and *w* were found to be negative [45].

Tan *et al.* used pyrolysis to synthesise CQDs from water hyacinth and optimised the same parameters. Similarly, they observed positive linear and interaction coefficients with high significance. All three quadratic parameters were negative [46]. Detailed comparisons of the results of the fitting of the experimental design, according to Eq. (2), between the present and the other two studies exploring the same factors are represented in Table 6.

[a]) this work; [b]) the high values are because the authors used maximum emission intensity values for the construction of the experimental design.

Fig. 4(a) and (b) show the predicted *Φ* values and residues, respectively, as a function of the experimental data showing a good mutual agreement, with higher uncertainty for experiment 17, which featured the highest *Φ* value.

The predicted quantum yield at the central point of the experimental domain (where all factors are set to level 0, corresponding to $w =$ 250 mg, $T = 180$ °C, and $t = 6$ h) was (0.91 ± 0.04) %. The experimental values (from experiments 10–13) were (0.80 ± 0.07) %. The Student's *t*-test ($t = (\Phi_{\text{experimental}} - \Phi_{\text{predicted}}) \,/\, SD_{\text{pooled}} =$ -1.57, where $SD_{\text{pooled}} = \sigma^2$ from Eq. 3) indicated no statistically-significant difference between the experimentally determined quantum yield and the model-predicted value, thus validating the model.

3.2. Optical properties

The study of the optical properties of CQD water solutions is essential for evaluating their potential use as sensors, providing insights into their photoluminescence efficiency and structural features.

The absorption spectrum of the solution obtained from experiment 6 (black line in Fig. 5(a)) exhibited the typical features of a CQD UV–visible absorption profile, with a prominent shoulder around 280 nm. This band corresponds to the electronic transitions from the bonding π orbital to the antibonding π* orbital of the graphitic sp^2-hybridised carbon core. Additionally, another less pronounced shoulder was observed around 355 nm, attributed to the electronic transition from the non-bonding n

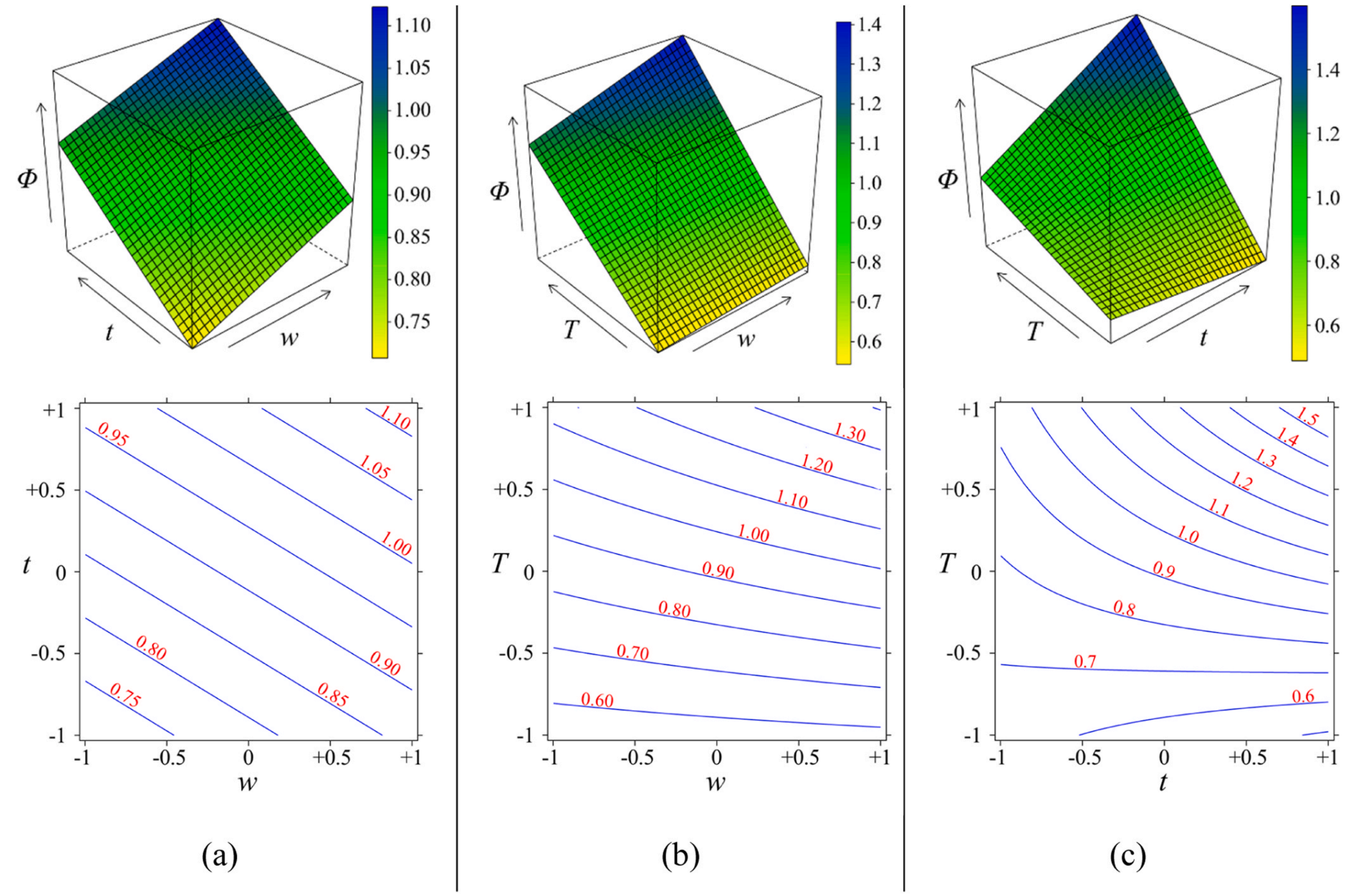

(a)

(b)

(c)

Fig. 1. Response surfaces of *Φ* (%) as a function of (a) time (*t*) and BP quantity (*w*), (b) temperature (*T*) and BP quantity (*w*), and (c) reaction temperature (*T*) and time (*t*) obtained from model 7. The third variable of each graph was kept constant at the central point.

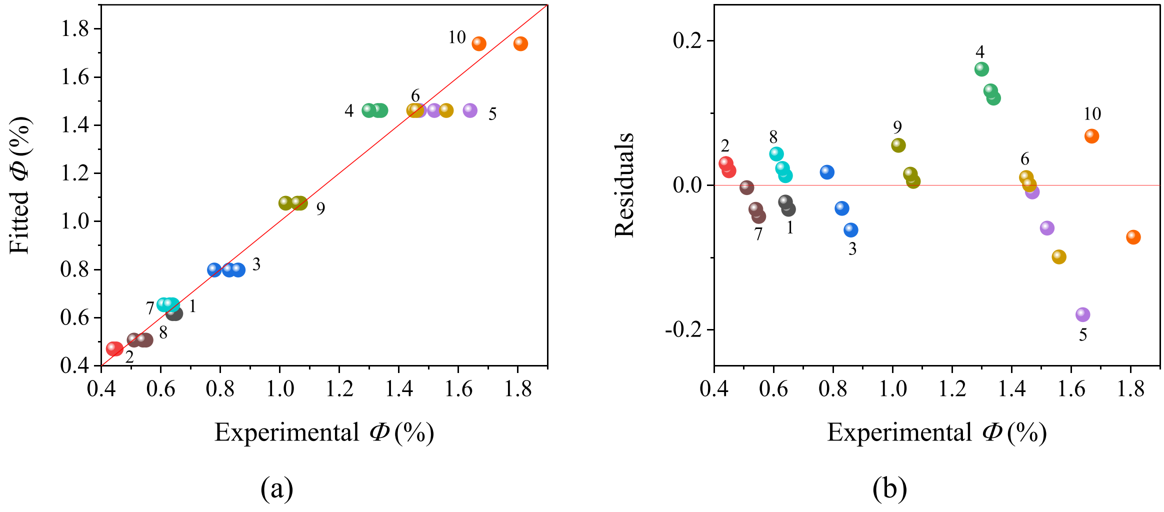

Fig. 2. (a) *Φ* values predicted by model 7 as a function of experimental *Φ*. (b) Residuals of the fitting.

to the antibonding π* orbitals of the C═O bonds [64,65].

These observations provided preliminary evidence for the formation of CQDs following hydrothermal treatment, strongly supported by the presence of a UV-stimulated fluorescence (blue line in Fig. 5(a); $\lambda_{ex} = 355$ nm) characterised by a broad emission band centred around 440 nm. The relative excitation spectrum (red line in Fig. 5(a); $\lambda_{em} = 440$ nm) presented a maximum at around 355 nm, closely matching the absorption shoulder at the same wavelength.

Similar observations could be made for the other samples with their absorption, emission, and excitation spectra (see Figure S2), with some differences among the profiles emerging especially when comparing samples prepared at different reaction temperatures. Solutions obtained by heating at 150 °C (experiments 1, 2, 7, 8 in Table 1) exhibited a more pronounced shoulder at 280 nm, followed by those synthesised at 180 °C (experiments 11–15 in Table 1). The 280 nm band was less evident in samples prepared at 210 °C (experiments 3–6, 9, 10, 16 in Table 1),

Table 4
Additional experiments of the experimental matrix with the three factors, the corresponding levels, and experimentally determined Φ values.

Experiment	w (mg)	t (h)	T (°C)	w	t	T	Φ (%)
14	250	9	180	0	+ 1	0	0.89 0.92 0.94
15	300	9	180	+ 1	+ 1	0	1.18 1.31 1.34
16	200	18	210	−1	+ 4	+ 1	1.64 1.65 1.68
17	450	15	210	+ 4	+ 3	+ 1	3.72 3.27 3.24

Table 5
Coefficients obtained from the fitting of model 53, their confidence interval and significance.

Coefficient	Value	Confidence interval	p-value
b_0	0.91	0.04	< 0.001
b_1	0.09	0.04	< 0.001
b_2	0.14	0.04	< 0.001
b_3	0.35	0.04	< 0.001
b_{13}	0.06	0.04	0.0069
b_{23}	0.21	0.04	< 0.001
b_{11}	0.06	0.02	< 0.001
b_{22}	−0.05	0.02	< 0.001

except for experiment 17, which had the highest Φ. In this case, the shoulder at 280 nm was also visually evident.

Emission spectra were also registered as a function of the excitation wavelength and reported in Fig. 5(b) and (c). It was possible to observe how the maximum emission wavelength shifted to longer wavelengths while increasing the excitation wavelength, which is a well-known feature of CQDs. Although this behaviour is still under investigation [66,67], it is generally attributed to the size distribution of the carbon nanoparticles [68,69]. The same trend was observed for all synthesised samples.

The stability of the synthesised CQDs and their optical properties in aqueous solution will be assessed, together with the biocompatibility, for exploring their possible applications as biosensors.

In the following sections, samples are designated by their experiment number (corresponding to the synthesis conditions detailed in Table 1), followed by a letter indicating the synthesis batch. For example, samples 4b, 4c, and 4d were synthesised according to the experimental conditions specified for sample 4, but are not included in the overall experimental design. Due to the limited yield of CQDs from each synthesis, some characterisations were performed on different batches, taking advantage of the proven reproducibility of the synthetic protocol.

3.3. Surface enhanced raman scattering measurements

SERS measurements were carried out to confirm the successful formation of CQDs deposited onto previously prepared SERS-active substrates.

Fig. 6 reports the SERS spectra collected for 4b, 10b, and 11b, in the wavenumber range of 1250 cm^{-1} to 1650 cm^{-1}. The two characteristic

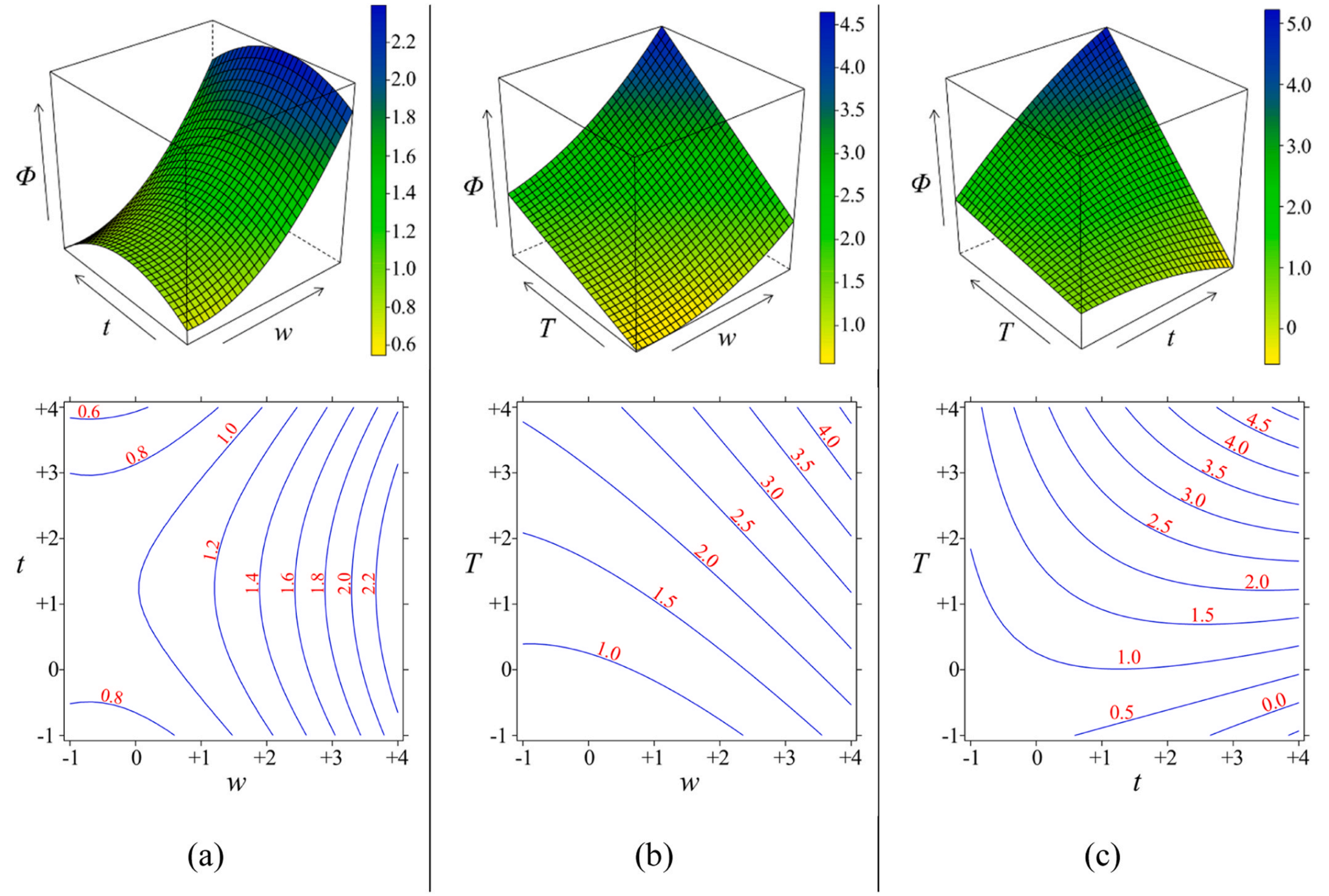

Fig. 3. Response surfaces of Φ (%) as a function of (a) time (t) and BP quantity (w), (b) temperature (T) and BP quantity (w), and (c) reaction temperature (T) and time (t) obtained from model 53. The third variable of each graph was kept constant at the central point.

Table 6
Comparison of the results of the fitting of the experimental design, according to Eq. (2), between the present study and the two others exploring the same factors (*w*, *t*, and *T*), the corresponding precursors, synthesis methods, and factor values.

Precursor	Synthesis method	*w* (g)	*t* (h)	*T* (°C)	Equation	Ref.
BP	Hydrothermal	0.2, 0.25, 0.3, 0.45	3, 6, 9, 15, 18	150, 180, 210	$0.91097 + 0.091883\ w + 0.13504\ t + 0.35274\ T + 0.057473\ w\ T + 0.20767\ t\ T + 0.064633\ w^2 – 0.054487\ t^2$	t. w.[a])
Peanut shells	Pyrolysis	60, 70, 80, 90, 100	1, 2, 3, 4, 5	340, 360, 380, 400, 420	$257.77 + 1.55\ w + 1.04\ T + 0.44\ t\ T – 0.0058\ w^2 – 0.0013\ T^2$	[45]
Water hyacinth	Pyrolysis	0.3, 0.5, 0.7	6, 8, 10	180, 200, 220	$43852.7 + 749.06\ w + 3282.6\ t + 5873.49\ T + 31.25\ w\ T + 156.87\ w\ t + 19.18\ t\ T – 3893.37\ w^2 – 9206.25\ t^2 - 17608.78\ T^2$ [b)]	[46]

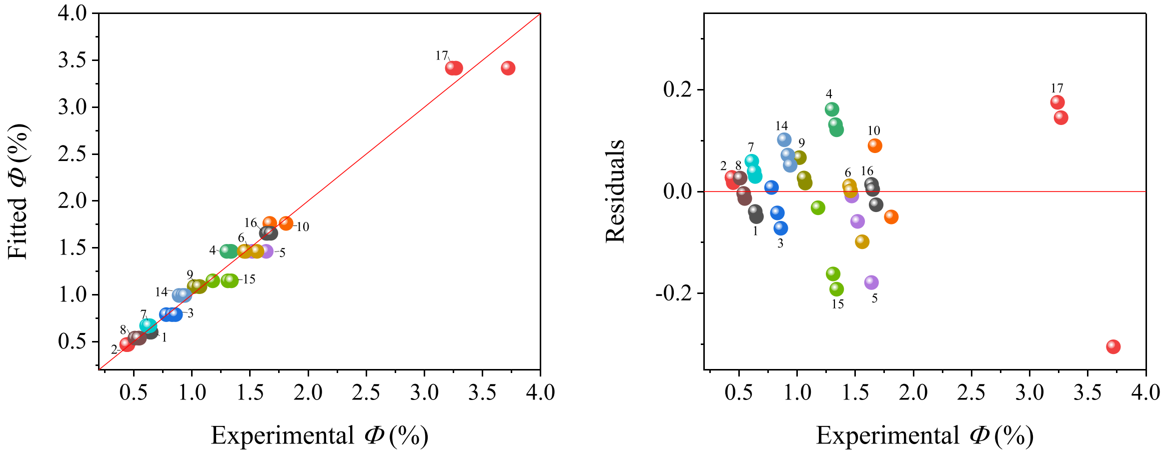

(a)   (b)

Fig. 4. (a) *Φ* values predicted by model 53 as a function of experimental *Φ*. (b) Residuals of the fitting.

D (at ~ 1386 cm^{-1}) and *G* (at ~ 1537 cm^{-1}) graphite bands are discernible in all investigated samples. These bands are respectively attributed to the disordered graphite with $A_{1\ g}$ symmetry (sp^3 hybridisation) and to graphite-type lattice vibrations (in-plane vibrational modes) with $E_{2\ g}$ symmetry (sp^2 hybridisation) [70].

Such an occurrence highlights a mixed sp^2/sp^3 carbon composition in which graphitic nanodomains are dispersed within an amorphous carbon matrix, supporting the presence of CQDs onto the prepared SERS substrates.

To understand how CQD synthesis parameters influence their formation mechanism by tracking the evolution of specific spectral features, a quantitative analysis of the 1280–1600 cm^{-1} range was performed using a five-peak curve-fitting model [71,72]. As widely reported [73–75], the aforementioned spectral region is known to contain not only the typical *D* and *G* bands but also overlapping signals indicative of defects and disorder within the graphitic lattice, as well as phonon-related modes reflecting variations in bonding, stacking order, and strain. Fig. 7 shows the results of applying this curve-fitting to the experimental SERS spectra of 4b, 10b, and 11b in the 1280–1600 cm^{-1} range.

The assignment of the deconvoluted sub-bands was based on the literature [71,72,76]. The predominant *D* and *G* vibrational bands were identified with mean position across the three preparations at approximately 1392 cm^{-1} and 1540 cm^{-1}, respectively. The *D** sub-band, centred at ~ 1371 cm^{-1}, corresponded to sp^2/sp^3 bond vibrations within the carbon dot core/shell. This band appeared blue-shifted compared to its typical position in common carbon-based materials [77,78], indicating a reinforcement of the dipole moment likely due to double resonance effects and quantum confinement. Finally, the *D'* and *D''* sub-bands, located at ~ 1472 cm^{-1} and ~ 1515 cm^{-1}, respectively, can be related to the local organisation of amorphous carbon in interstitial sites of the graphite-type lattice (*D'*) and to impurities and oxygen-related defects within the CQD carbon core (*D''*).

From the best-fit, the relative intensity ratio of the *D* band to the G band (I_D/I_G), which reflects the degree and density of defects within the CQD network, was calculated for each sample under investigation. The resulting values were 1.7, 1.5, and 1.4 for samples 4b, 10b, and 11b, respectively, indicating the presence of structural defects in all CQDs. The calculated ratios suggest a structure featuring confined sp^2 domains dispersed within a largely sp^3 matrix, with a marked tendency to amorphisation [79].

As widely reported [80–82], within the framework of the Tuinstra–Koenig model [83], the I_D/I_G ratio is linearly dependent on the reciprocal of the CQD grain size (L_{gs}), following Eq. 7:

$$L_{gs}(nm) = \frac{560}{E^4_{laser}}\left(\frac{I_D}{I_G}\right)^{-1} = (2.37 \times 10^{-10})\ \lambda^4_{laser}\left(\frac{I_D}{I_G}\right)^{-1} \tag{7}$$

with E_{laser} and λ_{laser} being the energy and wavelength of the excitation laser source, respectively.

Based on the calculated I_D/I_G ratios and our laser excitation wavelength of 785 nm, the estimated mean diameters were 52.94 nm (4b), 60.00 nm (10b), and 62.28 nm (11b).

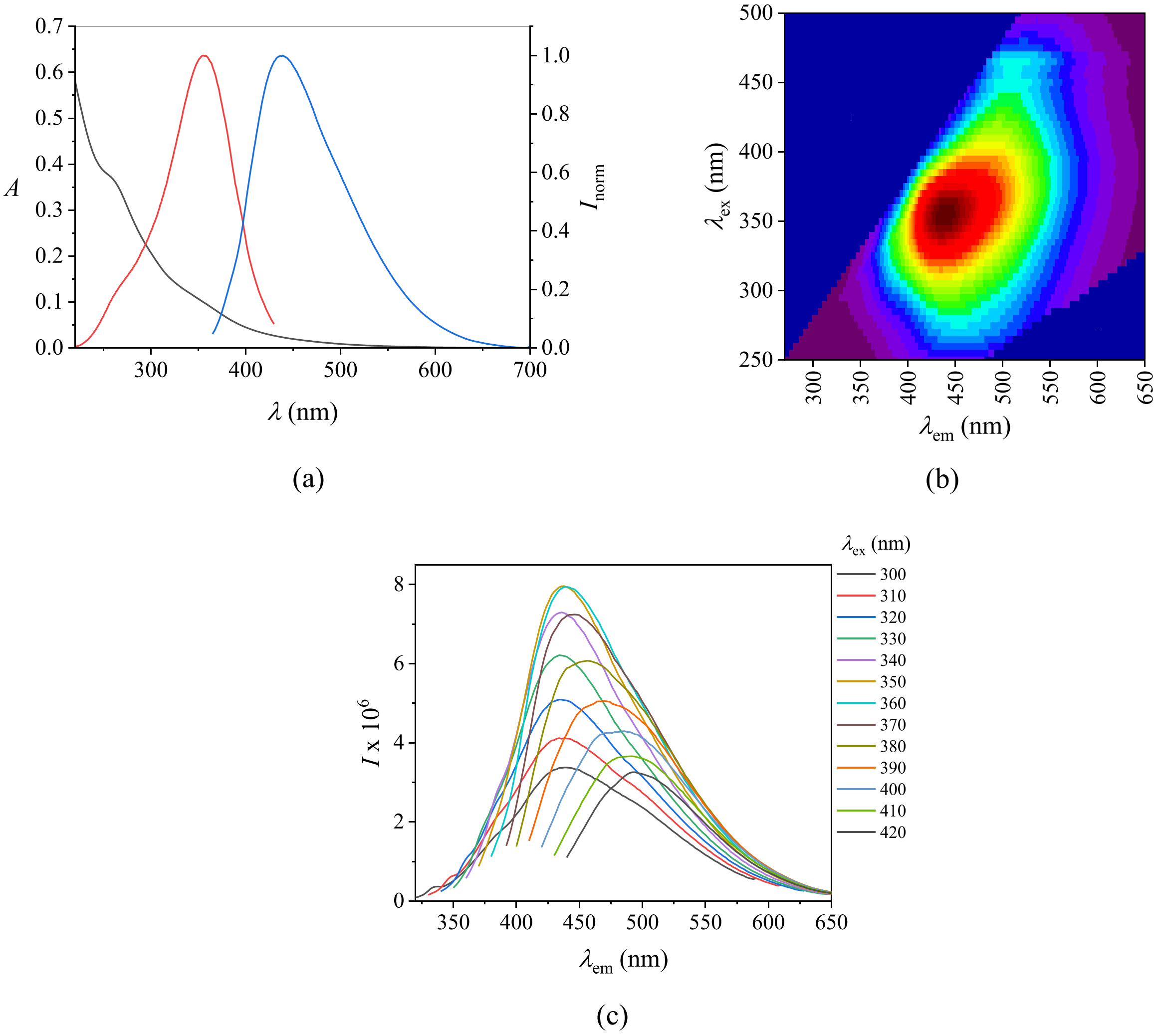

Fig. 5. (a) UV–visible absorption spectrum (black line), normalised emission (blue line), and excitation (red line) spectra of CQDs from experiment 6. (b) Excitation-emission map of CQDs. (c) Emission spectra recorded as a function of the excitation wavelength.

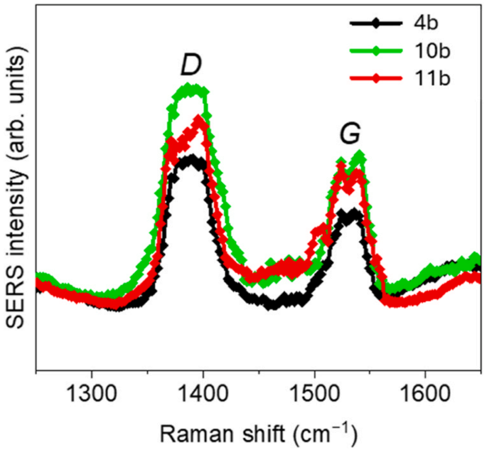

Fig. 6. Experimental SERS spectra of synthesised CQDs, recorded in the 1250 cm^{-1}–1650 cm^{-1} range, with the indication of the D- and G-bands position.

The intensity of the *D'* sub-band increased from 4b to 11b, suggesting a growing population of amorphous carbon within interstitial sites and highlighting a strong influence of the synthesis parameters on the stabilisation/organisation of carbon domains.

Finally, the significant contribution of the *D''* sub-band across all the investigated samples indicates a significant amount of carbon defects introduced during the synthesis process.

3.4. Transmission electron microscopy (TEM) measurements

TEM measurements were conducted to assess the particle size of CQDs in three representative samples, namely 6, 8, and 12. Sample 6 (Fig. 8(a)), which had a $\Phi = (1.5 \pm 0.1)$ % and was synthesised at 210 °C for 9 h, exhibited particles of varying shapes and sizes. Specifically, particles with diameters of approximately 10, 20, and 40 nm were consistently observed across different regions of the sample holder.

Sample 8 (Fig. 8(b)) synthesised at 150 °C and displaying one of the lowest $\Phi = (0.53 \pm 0.02)$ %, predominantly consisted of spherical particles of ~ 20 nm (mean 24.2 nm, SD = 3.5 nm), with higher homogeneity in shape and size compared to sample 6.

Sample 12 (Fig. 8(c)), corresponding to the central point of the experimental domain, also showed homogeneous spherical particles, with a main particle diameter of ~ 50 nm (52.5 nm, SD = 6.7 nm) and the presence of some smaller particles of ~ 20 nm.

The particle size for samples synthesised under the same conditions of 6 and 12 is lower than those estimated by SERS for samples 4b and 11b, respectively, with a difference of ~ 10 nm for both samples.

These results indicate that the synthesis parameters influence the

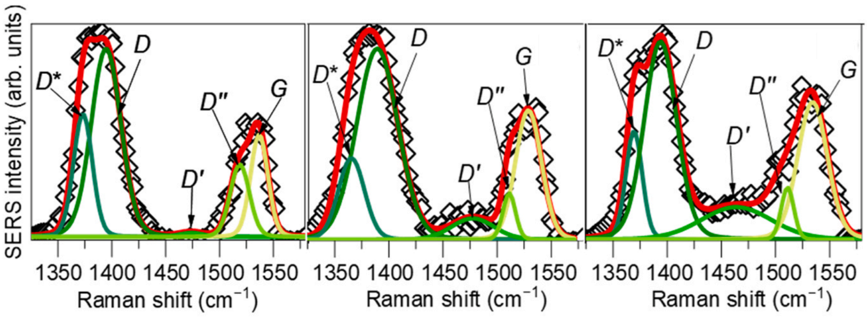

(a) (b) (c)

Fig. 7. Best-fit results for the SERS spectra of (a) 4b, (b) 10b, and (c) 11b in the 1280–1600 cm^{-1} region. The experimental data are represented by diamonds, the best-fit by red lines, and the individual deconvolution components by differently hued green bands. See text for further details.

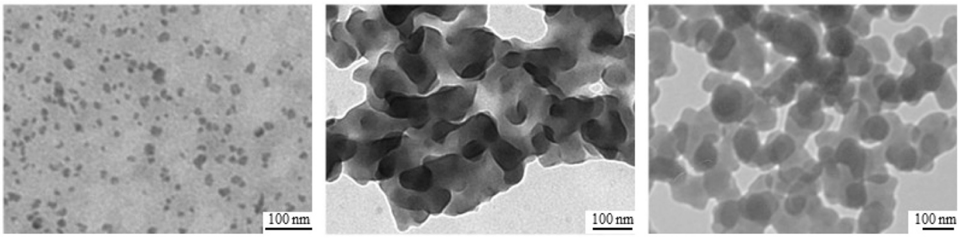

(a) (b) (c)

Fig. 8. TEM images of samples (a) 6, (b) 8, and (c) 12. The black lines indicate the scale.

size and shape of the resulting CQDs. When the highest temperature is used for the hydrothermal treatment, the particle shape appears more heterogeneous. Nevertheless, a more notable population of 10 nm particles (most typical for CQDs) is observed. In contrast, the use of lower temperatures led to the formation of more spherical nanoparticles with larger average sizes. This behaviour may result from the stepwise thermal degradation of different *BP* components, as demonstrated by Raccuia *et al.* through thermogravimetric analysis of the same biomass used in this study [84]. The degradation of multiple components at elevated temperatures could contribute to the formation of CQDs with varying particle size.

Although the CQDs under study exceed the typical sizes (< 10 nm), several examples have been reported of carbon nanoparticles with larger diameters. For example, sizes up to ~60 nm were observed [85–95]. Notably, the hydrothermal treatment of citrus fruits, such as lemon or grapefruit extracts, at 180 °C for 6 h, yielded CQDs with diameters of ~ 50 nm and < 30 nm, respectively [94].

3.5. Light scattering measurements

The size and ζ-potential of 10c were determined *via* Dynamic Light Scattering (DLS) on solutions filtered through 0.22 μm membranes. The measurements, minimally affected by nanoparticle fluorescence, yielded a *Z* average diameter of (130 ± 2) nm and a ζ-potential of (-18 ± 1) mV (Fig. 9).

Given the large values obtained for the CQDs diameter, other experiments were conducted to try and improve the dispersion of the nanoparticles in solution, by treating the samples with ultrasounds

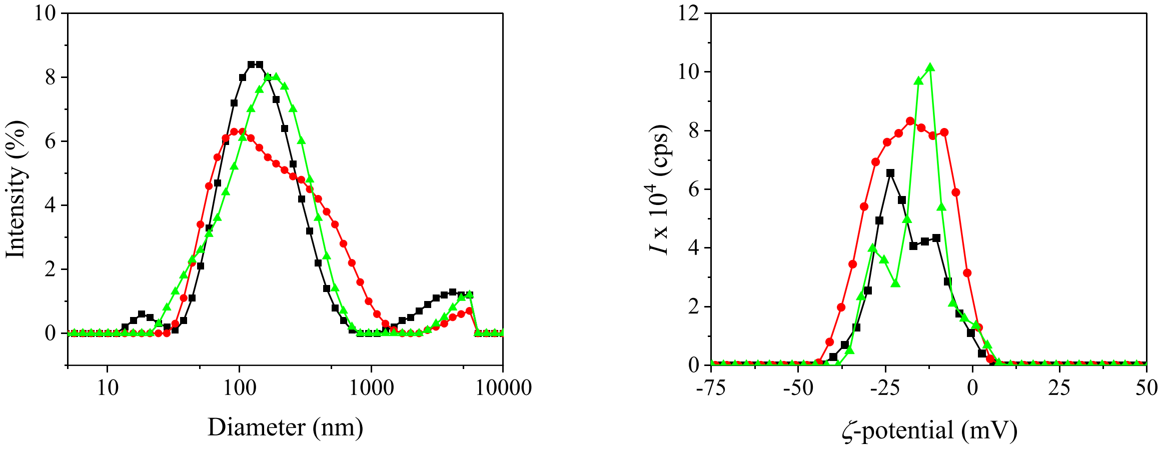

(a) (b)

Fig. 9. (a) Size and (b) ζ-potential of 10c determined via DLS.

(10 min in an ultrasound bath at a frequency of 40 Hz and a power of 120 W), or by adding small amount of acetone, a less polar solvent, before the DLS measurements. Average size after sonication was slightly reduced from 140 nm to 110 nm, further indicating a certain extent of particle aggregation. However, essentially neither approach yielded a reduced size of the suspended particles, leading to higher sample polydispersity and larger diameters (Figure S3), especially for samples treated with acetone. This evidence, together with the known ability of ultrasound to influence the size of carbon nanomaterials [96–98], led to the avoidance of pursuing both these strategies.

On the one hand, the larger hydrodynamic diameter measured by DLS compared to the size observed by TEM or estimated by SERS is not unexpected. DLS assesses the hydrodynamic radius, which includes the particle's hydration shell, likely leading to values significantly larger than those obtained by techniques sensitive to the core particle [99]. On the other hand, the low ζ-potential characterizing the nanoparticles does not allow us to rule out the presence of CQD supramolecular aggregates [100], whose size might be constrained by extrusion through the filter pores. Anyhow, the presence of nanoparticles with a size comparable to the exciton Bohr radius, namely of a few nanometers, is confirmed by the observed CQDs photoluminescence, which relies on quantum confinement effects [101,102].

3.6. CQDs purification via high performance liquid chromatography (HPLC)

Among the strategies employed for the purification of CQDs, HPLC enables the separation of the carbon nanoparticles from the synthesis by-products along with their characterisation [103,104].

In this study, the initial purification was carried out through dialysis and filtration. Further purification of CQDs was conducted by normal-phase (NP)-HPLC for experiments 4c, 9c, and 11c.

Fig. 10 shows the NP-HPLC chromatograms obtained for sample 4c using UV (Fig. 10(a)) and fluorescence (Fig. 10(b)) detection. A prominent double peak with a retention time of ~ 2.5 min was observed, followed by a second broadened and less intense set of peaks centred at ~ 7.3 min.

A similar behaviour was reported by Michaud *et al.* [105], who studied CQDs derived from citric acid and cysteine hydrothermally treated with varying reaction time and temperature without any purification before HPLC separation. CQDs were separated on a silica column (250 mm × 4.6 mm i.d. × 5 µm d_p) and eluted using a gradient of acetonitrile and H_2O. The obtained results revealed the presence of different by-products and CQDs families, with an initial sharp and intense peak followed by a later eluting fraction. Both fractions exhibited the photoluminescence properties typical of CQDs. The first fraction was attributed to hydrophobic carbon cores, while the second contained CQDs functionalised with polar groups [105].

In this study, the highest intensity peak at ~ 2.5 min, eluting at the start of the H_2O gradient, might be attributed to a CQD family characteristic of a lower polarity surface. This differs from the second, less intense and broadened peak, which is characterised by a higher polarity CQD family. The formation of these two populations may originate from the degradation and carbonization of different components of BP. Thermogravimetric analysis revealed an initial decomposition of low-molecular-weight polysaccharides, followed by the degradation of lignin, hemicellulose, and pectin at higher temperatures [84]. Although the confined environment of the autoclave likely lowers the degradation temperatures, the stepwise decomposition of BP components may significantly influence the surface chemistry of the resulting CQDs, leading to variations in polarity.

The presence of aggregation phenomena suggested by DLS measurements is further supported by variations of the peak area between consecutive injections, as highlighted in Figure S4. Particularly, a peak area increment close to 60 % was observed for the first fraction (2.5 min) after 3 injections over 1 h.

To further investigate the separation outcomes, the two main fractions (highlighted in light blue in Fig. 10(a)) were collected separately, and their optical properties were studied. While the excitation and emission spectra (red and blue lines, respectively, in Fig. 11) showed similar shapes for both fractions and the original CQDs, minor differences were observed in their absorption spectra (black lines in Fig. 11). Specifically, the shoulder associated to the π-π* transition of the C═C bonds was more pronounced in the first and less polar collected fractions (Fig. 11(a)). This may suggest a more pronounced graphitic core and less functionalised particles [105].

Nonetheless, both fractions retained the characteristic excitation-dependent emission typical of CQDs (Fig. 12), indicating that they possess the same emission mechanisms. These observations show that the product consists exclusively of carbon nanoparticles, although two distinct families differing in polarity can be identified.

Φ was also determined for each fraction, the values being reported in Table 7. The first fractions consistently exhibited higher values, while the second showed lower ones. This is consistent with the known influence of surface functionalities on the quantum yield of the CQDs [106]. The observed difference in Φ values supports the presence of two distinct CQD populations with different surface chemistries. For example, Vinci and Colón observed that CQDs with a higher abundance of polar carbonyl groups on their surface exhibited lower Φ values than less polar CQDs [106]. Their findings align well with the observations made in the present work. The average Φ between the two fractions closely agreed with that of the CQDs before separation (cf. Table 2), indicating that both populations contribute to the overall optical properties of the product directly obtained from the hydrothermal treatment. Although a separation step may be useful to increase further the Φ of the biomass-based CQDs, the Experimental Design proposed in this work remains valid as the relative Φ variation trend is preserved after the HPLC separation.

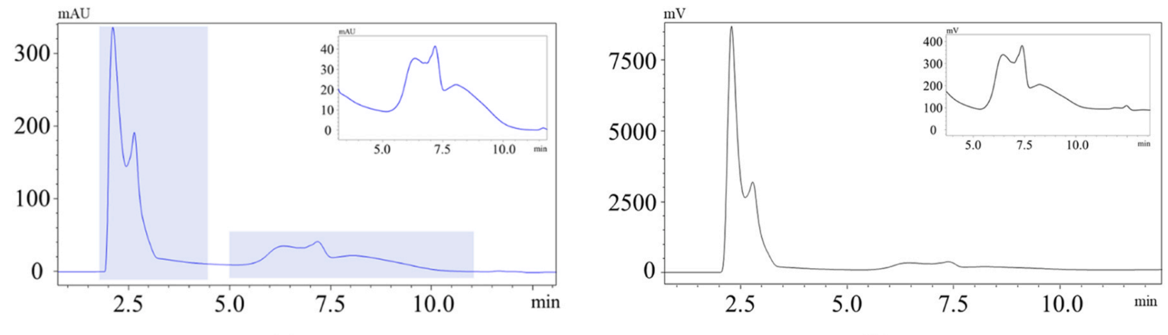

(a) (b)

Fig. 10.. Chromatograms of 4c separated through NP-HPLC. (a) UV detection at 280 nm. (b) Fluorescence detection at 450 nm with $\lambda_{ex} = 350$ nm.

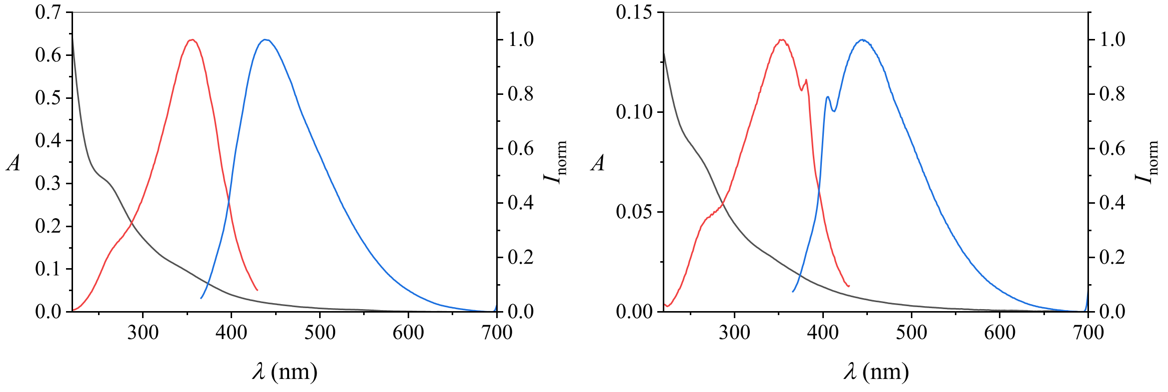

(a) (b)

Fig. 11. UV–visible absorption (black line), normalised excitation (red line), and emission (blue line) spectra of 4c separated by NP-HPLC. (a) First fraction. (b) Second fraction.

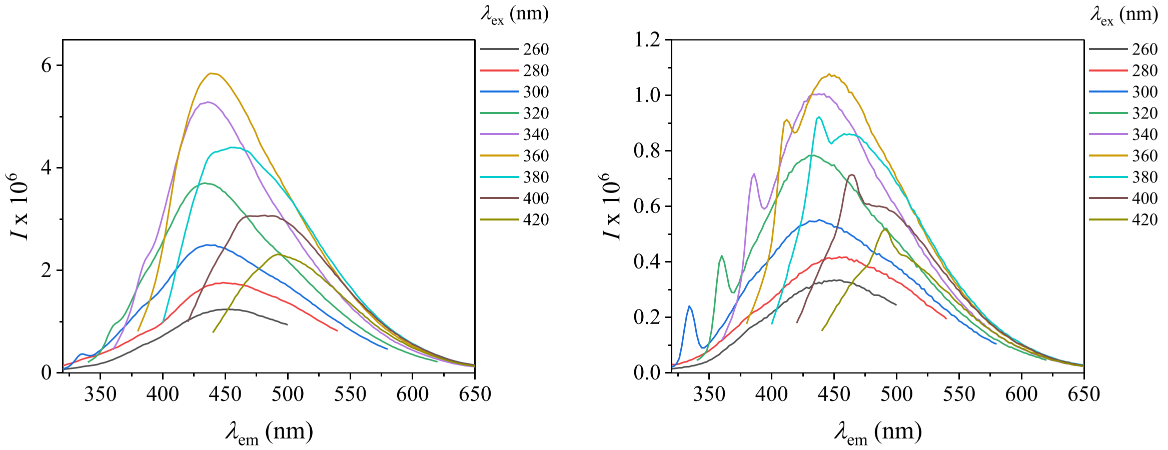

(a) (b)

Fig. 12. Emission spectra as a function of the excitation wavelength of 4c separated by NP-HPLC. (a) First fraction. (b) Second fraction.

Table 7
Quantum yields of CQDs: before HPLC separation, for individual HPLC-separated fractions, along with the average Φ of the separated fractions.

Experiment	Before separation Φ (%)	First fraction Φ (%)	Second fraction Φ (%)	Average Φ (%)
4c	1.5 ± 0.1	2.1 ± 0.1	1.24 ± 0.08	1.7 ± 0.1
9c	0.53 ± 0.01	0.79 ± 0.06	0.57 ± 0.03	0.68 ± 0.05
11c	0.80 ± 0.07	1.11 ± 0.06	0.52 ± 0.03	0.82 ± 0.05

3.7. *Attenuated total reflectance in fourier transform infrared spectroscopy (ATR-FTIR) measurements*

Infrared spectroscopy provides valuable insights into the structure of CQDs, particularly concerning their surface functional groups [20,31,87,107,108]. ATR-FTIR spectra were registered for all samples from the first set of experiments in the experimental design. Concentrated solutions were deposited onto aluminium foil and allowed to dry. Most formed a thin brownish film on the foil, which was analysed by contacting the foil with the ATR crystal. Two samples (experiments 1 and 7) formed a solid residue that could be removed from the aluminium foil and directly deposited onto the ATR diamond for spectrum acquisition. This difference was also reflected in the spectra of the latter two samples, which exhibited substantial variations compared to the other ones.

Fig. 13 presents the spectra for samples 1 and 4 as representative examples, and Table 8 lists the characteristic band wavenumbers. The profiles of all other samples are provided in Figure S5. Bands corresponding to O-H stretching vibrations were consistently observed at 3345–3384 cm^{-1} alongside the C-H stretching vibrations at 2938–2980 cm^{-1} [19,62,109,110].

Samples 1 and 7, synthesised under the lowest temperature and shortest reaction time, exhibited spectra similar to that of raw BP [49], indicating incomplete carbonisation of the starting material. Sample 1 (Fig. 13(a)) showed well-resolved bands in the above-mentioned region, along with peaks at 1731 and 1609 cm^{-1}, which were attributed to the stretching of non-ionic C═O double bonds (carboxyl or ester groups) and ionic carboxylate groups, respectively. The peak at 1415 cm^{-1} was assigned to the symmetric stretching vibration of COO^{-}. Peaks at 1247, 1073, and 1028 cm^{-1} could be related to the C-O stretching of carboxylic acids, alcohols, or ethers [49]. Similar observations were made for sample 7.

In contrast, the remaining samples that formed the film on the aluminium foil exhibited broad bands in the region below 1800 cm^{-1}. These were attributed to the overlapping of several vibration modes of the graphitic core of the CQDs and their surface functional groups.

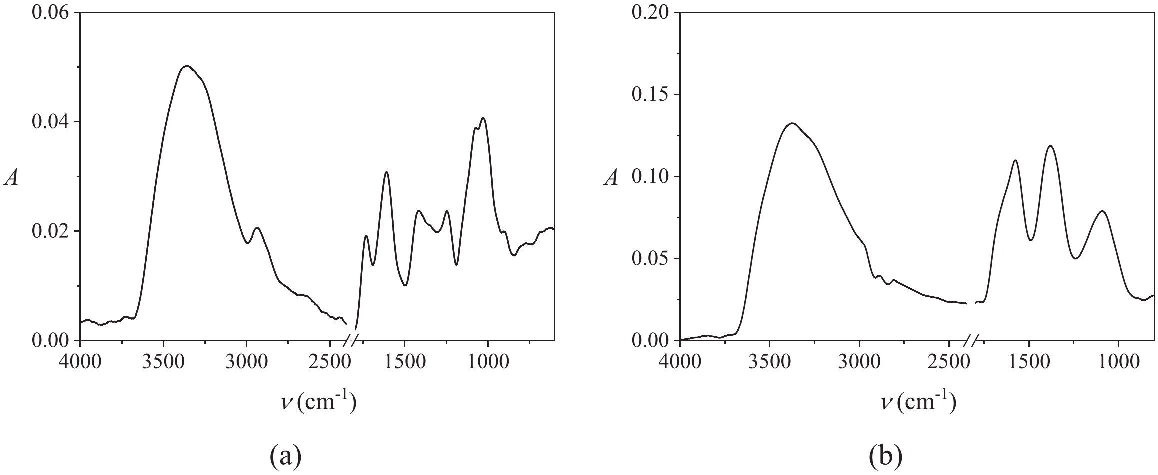

(a) (b)

Fig. 13. ATR-FTIR spectra of samples (a) 1 and (b) 4.

Table 8
Selected characteristic ATR-FTIR bands of CQDs.

Experiment	$\nu_{O\text{-}H}$ (cm^{-1})	$\nu_{C\text{-}H}$ (cm^{-1})	$\nu_{C{=}O}$ (cm^{-1})	$\nu_{C{=}C}$ (cm^{-1})	$\nu_{C\text{-}O}$ (cm^{-1})
1	3356	2939	1731, 1609	-	1247, 1073, 1028
2	3351	~ 2973	~ 1682	1579	1377, 1105
3	3348	~ 2971	~ 1678	1577	1390, 1109
4	3383	~ 2973	~ 1663	1580	1383, 1093
5	3384	~ 2977	~ 1658	1583	1378, 1104
6	3384	~ 2980	~ 1659	1583	1384, 1103
7	3367	2938	1732, 1614	-	1246, 1075, 1028
8	3355	~ 2963	~ 1698	1573	1381, 1037
9	3350	~ 2978	~ 1665	1573	1384, 1023
10	3354	~ 2956	~ 1684	1571	1386, 1093
11	3374	~ 2979	~ 1677	1576	1393, 1032
12	3349	~ 2979	~ 1673	1573	1384, 1022
13	3345	~ 2979	~ 1663	1578	1383, 1039

Spectra were similar for all studied samples, with slight differences in the relative intensities between the signals.

For instance, sample 4 (Fig. 13(b)) presented a prominent band at 1580 cm^{-1}, which could be attributed to the stretching of the double C=C bond in the graphitic core [59,111,112]. The band corresponding to the C=O stretching appeared as a shoulder around 1663 cm^{-1} [112–114]. The signal at 1383 cm^{-1} was assigned to the stretching vibrations of the single C-O bonds in carboxylic groups, along with the C-O-H bending mode of alcohols and alkyl C-H vibrations. The band at 1093 cm^{-1} could be assigned to the alcoholic and ether C-O stretching vibration [19,59,107].

Further evidence of the reproducibility of the synthesis procedure was provided by the similar ATR-FTIR spectra obtained for samples 4–6, all prepared under identical conditions, and similarly for samples 11–13, also prepared identically.

3.8. CQDs acid-base properties

The acid-base properties of three samples 4d, 10d, and 15d, obtained by diluting stock solutions (see Materials and Methods), were investigated by potentiometry at $I = 0.10$ mol dm^{-3} NaCl$_{(aq)}$, $T = 25$°C, and across the 2.0–11.0 pH range. The analysis of experimental data by means of the BSTAC program [57] revealed the identification of a single protonable active site, arbitrarily indicated as a mono-negatively charged group (X$^-$ site in Eq. 4). Its acidic constants and concentrations are reported in Table 8. The c_{site} values were calculated as the ratio of the diluted solutions concentration (in g dm^{-3}) to the software-refined concentration (in meq dm^{-3}). Table 9 also lists the initial *BP* mass, reaction time, and temperature employed for each CQD synthesis, as well as the average quantum yields (Φ_a (%)) calculated from the data in Table 2.

^{a}) logK^{H} related to the equilibrium in Eq. 4; ^{b}) value calculated for each sample as arithmetical average of the experimental Φ (%) reported in Table 2 for experiments n. 4d, 10d, and 15d, respectively, ^{c}) ± std. dev.

The refined logK^{H} values, potentially attributable to the ionisation of carboxylic groups [115] likely present on the CQDs surface under acidic conditions [116], showed good agreement across the different nanoparticles, with maximum discrepancies (ΔlogK^{H}) of around 0.65 logarithmic units between samples 4d and 10d. In addition, a decrease in logK^{H} values was observed with increasing precursor weight and synthesis temperature, the reaction time being the same for all considered CQDs. Furthermore, Table 9 highlights that the active site concentrations (c_{site} / meq g^{-1}) decreased with higher *BP* mass and lower reaction temperature. No clear correlation was evident between the determined parameters and Φ_a.

The determined acidic constants and active site concentrations (c_{site} / meq g^{-1}) values can be compared with data reported by Raccuia *et al.* [84], who used the same original bergamot pomace batch as in this study. The authors determined values of logK^{H} $= 3.43$ and c_{site} $= 1.10$ meq g^{-1} at $I = 0.10$ mol dm^{-3} NaNO$_{3(aq)}$ and $T = 25$ °C, following a water pretreatment of the dried biomass. Further comparisons can be made with acid-base properties studied for CQDs derived from other biomasses [117,118] or citric acid-based samples [27,119]. Cabral Araújo *et al.* ù prepared highly hydrophilic carbon dots (HCDs) by dehydrating 5 g of cotton cellulose with H_2SO_4 at 80 °C for 40 min, followed by HNO_3 oxidation under reflux for 12 h and neutralisation with Na_2CO_3. Potentiometric measurements conducted without an ionic medium at $T = 25$ °C and in a 0.002 mol dm^{-3} HCl solution revealed three potential classes of oxygenated active sites, including carboxylic and phenolic groups, with logK^{H} < 5.0, $5.0 <$ logK^{H} < 8.0 and logK^{H} > 9.0, as well as $c_{\text{site}} = 3.20$, 0.54, 0.57 meq g^{-1}, respectively. Using the same synthetic procedure, Alves' research group [118] investigated the HCDs behaviour at $I = 0.10$ mol dm^{-3} NaCl$_{(aq)}$ and $T = 25$ °C. Their data analysis, employing a non-linear regression method based on the Levenberg–Marquardt algorithm, suggested the presence of oxygenated acidic sites with five ionisation constants logK^{H} = 3.59, 5.01, 6.19, 7.57, 9.30, and corresponding c_{site} = 1.88, 1.13, 0.39, 0.24, 0.96 meq g^{-1}. Wang *et al.* [27] hydrothermally synthesised carbon quantum dots from citric acid (9.6 mg) and glycine (7.5 mg) at $T = 180$ °C for $t = 6$ h. Potentiometric studies of CQDs acid-base properties at $I = 0.10$ mol dm^{-3} NaClO$_{4(aq)}$ and $T = 25$ °C indicated the presence of two independent protonable groups, S and W, with acidic constants

Table 9
Protonation constants$^{a)}$ and active site concentrations determined at $I = 0.10$ mol dm^{-3} NaCl$_{(aq)}$ and $T = 25$°C for selected CQDs samples, together with the corresponding w, t, and T factors, levels, and average Φ_a (%)$^{b)}$ values.

Sample	$\log K^{H\ a)}$	c_{site} (meq g^{-1})	Φ_a (%)$^{b)}$	w (mg)	t (h)	T (°C)	w	t	T
4d	4.60 ± 0.04$^{c)}$	4.92	1.5 ± 0.1$^{c)}$	200	9	210	−1	+ 1	+ 1
10d	3.95 ± 0.11	3.70	1.76 ± 0.08	300	9	210	+ 1	+ 1	+ 1
15d	4.44 ± 0.06	3.25	1.28 ± 0.09	300	9	180	+ 1	+ 1	0

$\log K^H_S = 2.16$ and $\log K^H_W = 4.98$, and sites concentrations $c_S = 6.76$ meq g^{-1} and $c_W = 2.74$ meq g^{-1}. Wu and colleagues [119] synthesised N-doped graphene quantum dots from 70 mg citric acid and 250 mg dicyandiamide at $T = 180$°C and $t = 3$ h. Two acidic constants were refined at pH > 3.0, namely $\log K^H = 4.28$ and 5.21.

4. Conclusions

This study employed for the first time a full factorial experimental design to optimise the hydrothermal synthesis of biomass-based CQDs, systematically evaluating the influence of biomass quantity, reaction time, and temperature on the quantum yield and achieving a Φ of (3.4 ± 0.3) %. The validated model included quadratic terms for biomass quantity (positive) and reaction time (negative), identifying approximately 9 h as optimal to obtain the highest Φs. The results highlight the importance of a preliminary systematic screening of the combined effect of the synthesis parameters to improve the properties of CQDs.

The multi-technique characterisation confirmed the formation of CQDs featuring the typical optical properties and characterised by the presence of carboxylic groups on their surface. The particle size, obtained from TEM images, ranged from 10 to ~ 50 nm depending on the synthesis condition. Large hydrodynamic diameters ((130 ± 2) nm) and relatively low ζ-potential values ((-18 ± 1) mV) suggest the formation of supramolecular aggregates of the emissive carbon nanoparticles. This conclusion is corroborated also by HPLC, which led to the identification of two distinct CQD families differing in polarity.

Overall, this study demonstrates the added value of employing an experimental design approach rather than the most common one-variable-at-a-time method for optimising CQDs synthesis when considering the combined variable effects. The presented findings contribute to understanding CQD properties while presenting good practices for developing biocompatible nanomaterials from agricultural waste, aligning with circular economy principles and respecting the green chemistry guidelines.

CRediT authorship contribution statement

Emanuele Zanda: Writing – original draft, Resources, Investigation, Formal analysis, Data curation. **Eleonora Macedi:** Writing – original draft, Investigation, Formal analysis, Data curation. **Mauro Formica:** Writing – original draft, Validation, Supervision, Formal analysis. **Salvatore Giovanni Michele Raccuia:** Writing – original draft, Software, Investigation, Formal analysis, Data curation. **Concetta De Stefano:** Visualization, Validation, Supervision, Conceptualization. **Anna Irto:** Writing – original draft, Validation, Methodology, Formal analysis, Data curation, Conceptualization. **Valentina Venuti:** Writing – original draft, Visualization, Resources, Methodology, Conceptualization. **Clemente Bretti:** Visualization, Validation, Formal analysis, Data curation. **Luigi Mondello:** Visualization, Supervision, Methodology, Conceptualization. **Ileana Ielo:** Writing – original draft, Validation, Investigation, Formal analysis, Data curation. **Gabriele Lando:** Writing – review & editing, Supervision, Software, Project administration, Methodology, Funding acquisition, Conceptualization. **Giovanna De Luca:** Writing – review & editing, Visualization, Validation, Supervision, Methodology, Conceptualization. **CARDIANO Paola:** Writing – review & editing, Visualization, Supervision, Methodology, Funding acquisition, Conceptualization. **Alessia Arena:** Writing – original draft, Investigation, Formal analysis, Data curation. **Mariosimone Zoccali:** Writing – original draft, Validation, Methodology, Investigation, Conceptualization. **Francesco Caridi:** Software, Investigation, Formal analysis, Data curation. **Giuseppe Paladini:** Writing – original draft, Methodology, Investigation, Formal analysis, Data curation.

Declaration of Competing Interest

The authors declare that they have no known competing financial interests or personal relationships that could have appeared to influence the work reported in this paper.

Acknowledgements

This work was supported by Next Generation EU, Missione 4, Componente 1, CUP J53D23007540006—PRIN_2022HYH95P. The authors acknowledge the Shimadzu Corporation and Merck KGaA (Darmstadt, Germany) for their support.

Appendix A. Supporting information

Supplementary data associated with this article can be found in the online version at doi:10.1016/j.jece.2025.118472.

Data availability

Data will be made available on request.

References

[1] C. Liu, M. Wen, X. Zhou, X. Huang, S. Zhang, H. Liu, Starch-derived carbon dots with enhanced photoluminescence and tunable emission for multilevel anticounterfeiting, ACS Sustain. Chem. Eng. 12 (2024) 12354–12364, https://doi.org/10.1021/acssuschemeng.4c02499.

[2] R. Üzek, Engineering a graphene quantum dot-enhanced surface plasmon resonance sensor for ultra-sensitive detection of Hg2$^+$ ions, Adv. Mater. Interfaces 12 (2025) 2400679, https://doi.org/10.1002/admi.202400679.

[3] Y. Zhou, A. Camisasca, S. Dominguez-Gil, M. Bartkowski, K.D. Rochfort, M. Piletti, A. White, D. Krizsan, R. O'Connor, S.J. Quinn, D. Iacopino, A. J. Eustace, S. Giordani, Synthesis of carbon dots from spent coffee grounds: transforming waste into potential biomedical tools, Nanoscale 17 (2025) 9947–9962, https://doi.org/10.1039/D4NR05186F.

[4] X. Li, M. Rui, J. Song, Z. Shen, H. Zeng, Carbon and graphene quantum dots for optoelectronic and energy devices: a review, Adv. Funct. Mater. 25 (2015) 4929–4947, https://doi.org/10.1002/adfm.201501250.

[5] Z. Yang, T. Xu, H. Li, M. She, J. Chen, Z. Wang, S. Zhang, J. Li, Zero-dimensional carbon nanomaterials for fluorescent sensing and imaging, Chem. Rev. 123 (2023) 11047–11136, https://doi.org/10.1021/acs.chemrev.3c00186.

[6] G. Calabrese, G. De Luca, G. Nocito, M.G. Rizzo, S.P. Lombardo, G. Chisari, S. Forte, E.L. Sciuto, S. Conoci, Carbon dots: an innovative tool for drug delivery in brain tumors, Int. J. Mol. Sci. 22 (2021) 11783, https://doi.org/10.3390/ijms222111783.

[7] C.S. Lim, K. Hola, A. Ambrosi, R. Zboril, M. Pumera, Graphene and carbon quantum dots electrochemistry, Electrochem. Commun. 52 (2015) 75–79, https://doi.org/10.1016/j.elecom.2015.01.023.

[8] V. Georgakilas, J.A. Perman, J. Tucek, R. Zboril, Broad family of carbon nanoallotropes: classification, chemistry, and applications of fullerenes, carbon dots, nanotubes, graphene, nanodiamonds, and combined superstructures, Chem. Rev. 115 (2015) 4744–4822, https://doi.org/10.1021/cr500304f.

[9] J. Dhariwal, G.K. Rao, D. Vaya, Recent advancements towards the green synthesis of carbon quantum dots as an innovative and eco-friendly solution for metal ion sensing and monitoring, RSC Sustain. 2 (2024) 11–36, https://doi.org/10.1039/D3SU00375B.

[10] F. Yan, Y. Jiang, X. Sun, Z. Bai, Y. Zhang, X. Zhou, Surface modification and chemical functionalization of carbon dots: a review, Microchim. Acta 185 (2018) 424, https://doi.org/10.1007/s00604-018-2953-9.

[11] A.S. Karakoti, R. Shukla, R. Shanker, S. Singh, Surface functionalization of quantum dots for biological applications, Adv. Colloid Interface Sci. 215 (2015) 28–45, https://doi.org/10.1016/j.cis.2014.11.004.

[12] F. Arcudi, L. Đorđević, Supramolecular chemistry of carbon-based dots offers widespread opportunities, Small 19 (2023) 2300906, https://doi.org/10.1002/smll.202300906.

[13] X. Gao, C. Du, Z. Zhuang, W. Chen, Carbon quantum dot-based nanoprobes for metal ion detection, J. Mater. Chem. C. 4 (2016) 6927–6945, https://doi.org/10.1039/C6TC02055K.

[14] K.G. Nguyen, I.-A. Baragau, R. Gromicova, A. Nicolaev, S.A.J. Thomson, A. Rennie, N.P. Power, M.T. Sajjad, S. Kellici, Investigating the effect of N-doping on carbon quantum dots structure, optical properties and metal ion screening, Sci. Rep. 12 (2022) 13806, https://doi.org/10.1038/s41598-022-16893-x.

[15] Q. Xu, T. Kuang, Y. Liu, L. Cai, X. Peng, T. Sreenivasan Sreeprasad, P. Zhao, Z. Yu, N. Li, Heteroatom-doped carbon dots: synthesis, characterization, properties, photoluminescence mechanism and biological applications, J. Mater. Chem. B 4 (2016) 7204–7219, https://doi.org/10.1039/c6tb02131j.

[16] Q. Xu, P. Pu, J. Zhao, C. Dong, C. Gao, Y. Chen, J. Chen, Y. Liu, H. Zhou, Preparation of highly photoluminescent sulfur-doped carbon dots for Fe(III) detection, J. Mater. Chem. A 3 (2014) 542–546, https://doi.org/10.1039/C4TA05483K.

[17] X. Li, Y. Fu, S. Zhao, J. Xiao, M. Lan, B. Wang, K. Zhang, X. Song, L. Zeng, Metal ions-doped carbon dots: synthesis, properties, and applications, Chem. Eng. J. 430 (2022) 133101, https://doi.org/10.1016/j.cej.2021.133101.

[18] X. Xu, R. Ray, Y. Gu, H.J. Ploehn, L. Gearheart, K. Raker, W.A. Scrivens, Electrophoretic analysis and purification of fluorescent Single-Walled carbon nanotube fragments, J. Am. Chem. Soc. 126 (2004) 12736–12737, https://doi.org/10.1021/ja040082h.

[19] O. Dagdag, T.W. Quadri, W. Daoudi, E. Berdimurodov, H. Kim, Carbon nanodots: basics, properties, and fundamentals, in: Carbon Dots: Recent Developments and Future Perspectives, American Chemical Society, 2024, pp. 127–145, https://doi.org/10.1021/bk-2024-1465.ch006.

[20] J. Fan, L. Kang, X. Cheng, D. Liu, S. Zhang, Biomass-derived carbon dots and their sensing applications, Nanomaterials 12 (2022) 4473, https://doi.org/10.3390/nano12244473.

[21] Z.A. Qureshi, H. Dabash, D. Ponnamma, M.K.G. Abbas, Carbon dots as versatile nanomaterials in sensing and imaging: efficiency and beyond, Heliyon 10 (2024) e31634, https://doi.org/10.1016/j.heliyon.2024.e31634.

[22] R. Dhiman, J. Kumar, M. Singh, Fluorescent carbon dots for sensing applications: a review, Anal. Sci. 40 (2024) 1387–1396, https://doi.org/10.1007/s44211-024-00609-4.

[23] M.J. Molaei, Principles, mechanisms, and application of carbon quantum dots in sensors: a review, Anal. Methods 12 (2020) 1266–1287, https://doi.org/10.1039/C9AY02696G.

[24] H. Feng, Z. Qian, Functional carbon quantum dots: a versatile platform for chemosensing and biosensing, Chem. Rec. 18 (2018) 491–505, https://doi.org/10.1002/tcr.201700055.

[25] H. Shabbir, E. Csapó, M. Wojnicki, Carbon quantum dots: the role of surface functional groups and proposed mechanisms for metal ion sensing, Inorganics 11 (2023) 262, https://doi.org/10.3390/inorganics11060262.

[26] H.E. Emam, Carbon quantum dots derived from polysaccharides: chemistry and potential applications, Carbohydr. Polym. 324 (2024) 121503, https://doi.org/10.1016/j.carbpol.2023.121503.

[27] Z. Wang, Y. Xie, Z. Lei, Y. Lu, G. Wei, S. Liu, C. Xu, Z. Zhang, X. Wang, L. Rao, J. Chen, Quantitative analysis of surface sites on carbon dots and their interaction with metal ions by a potentiometric titration method, Anal. Chem. 91 (2019) 9690–9697, https://doi.org/10.1021/acs.analchem.9b01225.

[28] A. Kolanowska, G. Dzido, M. Krzywiecki, M.M. Tomczyk, D. Łukowiec, S. Ruczka, S. Boncel, Carbon quantum dots from amino acids revisited: survey of renewable precursors toward high Quantum-Yield blue and Green fluorescence, ACS Omega 7 (2022) 41165–41176, https://doi.org/10.1021/acsomega.2c04751.

[29] J. Ren, L. Malfatti, P. Innocenzi, Citric acid derived carbon dots, the challenge of understanding the Synthesis-Structure relationship, C 7 (2021) 2, https://doi.org/10.3390/c7010002.

[30] X. Wang, Y. Zhao, T. Wang, Y. Liang, X. Zhao, K. Tang, Y. Guan, H. Wang, Carboxyl-Rich carbon dots as highly selective and sensitive fluorescent sensor for detection of Fe3+ in water and lactoferrin, Polymers 13 (2021) 4317, https://doi.org/10.3390/polym13244317.

[31] M. Hamed, S. Chinnam, A. Bedair, S. Emara, F.R. Mansour, Carbon quantum dots from natural sources as sustainable probes for metal ion sensing: preparation, characterizations and applications, Talanta Open 10 (2024) 100348, https://doi.org/10.1016/j.talo.2024.100348.

[32] M. Palacio-Vergara, M. Álvarez-Gómez, J. Gallego, D. López, Biomass solvothermal treatment methodologies to obtain carbon quantum dots: a systematic review, Talanta Open 8 (2023) 100244, https://doi.org/10.1016/j.talo.2023.100244.

[33] M. Kurian, A. Paul, Recent trends in the use of Green sources for carbon dot synthesis–A short review, Carbon Trends 3 (2021) 100032, https://doi.org/10.1016/j.cartre.2021.100032.

[34] S. Mathew, B. Mathew, A review on the synthesis, properties, and applications of biomass derived carbon dots, Inorg. Chem. Commun. 156 (2023) 111223, https://doi.org/10.1016/j.inoche.2023.111223.

[35] P. Anastas, N. Eghbali, Green chemistry: principles and practice, Chem. Soc. Rev. 39 (2009) 301–312, https://doi.org/10.1039/B918763B.

[36] J. Kirchherr, N.-H.N. Yang, F. Schulze-Spüntrup, M.J. Heerink, K. Hartley, Conceptualizing the circular economy (Revisited): an analysis of 221 definitions, Resour. Conserv. Recycl. 194 (2023) 107001, https://doi.org/10.1016/j.resconrec.2023.107001.

[37] R.S. Tade, S.N. Nangare, A.G. Patil, A. Pandey, P.K. Deshmukh, D.R. Patil, T. N. Agrawal, S. Mutalik, A.M. Patil, M.P. More, S.B. Bari, P.O. Patil, Recent advancement in Bio-precursor derived graphene quantum dots: synthesis, characterization and toxicological perspective, Nanotechnology 31 (2020) 292001, https://doi.org/10.1088/1361-6528/ab803e.

[38] J. Zhao, Y. Peng, K. Yang, Y. Chen, S. Zhao, Y.-M. Liu, A new ratiometric fluorescence assay based on resonance energy transfer between biomass quantum dots and organic dye for the detection of sulfur dioxide derivatives, RSC Adv. 9 (2019) 41955–41961, https://doi.org/10.1039/C9RA09437G.

[39] Y. Wu, Y. Li, X. Pan, C. Hu, J. Zhuang, X. Zhang, B. Lei, Y. Liu, Hemicellulose-triggered high-yield synthesis of carbon dots from biomass, N. J. Chem. 45 (2021) 5484–5490, https://doi.org/10.1039/D1NJ00340B.

[40] R. Leardi, Experimental design in chemistry: a tutorial, Anal. Chim. Acta 652 (2009) 161–172, https://doi.org/10.1016/j.aca.2009.06.015.

[41] M.A. Issa, Z.Z. Abidin, S. Sobri, S.A. Rashid, M.A. Mahdi, N.A. Ibrahim, Fluorescent recognition of Fe3+ in acidic environment by enhanced-quantum yield N-doped carbon dots: optimization of variables using central composite design, Sci. Rep. 10 (2020) 11710, https://doi.org/10.1038/s41598-020-68390-8.

[42] M. Abdullah Issa, Z.Z. Abidin, S. Sobri, S. Abdul-Rashid, M.A. Mahdi, N. A. Ibrahim, M.Y. Pudza, Fabrication, characterization and response surface method optimization for quantum efficiency of fluorescent nitrogen-doped carbon dots obtained from carboxymethylcellulose of oil palms empty fruit bunch, Chin. J. Chem. Eng. 28 (2020) 584–592, https://doi.org/10.1016/j.cjche.2019.04.003.

[43] Ma.I.S. Dela Cruz, N. Thongsai, M.D.G. de Luna, I. In, P. Paoprasert, Preparation of highly photoluminescent carbon dots from polyurethane: optimization using response surface methodology and selective detection of silver (I) ion, Colloids Surf. A Physicochem. Eng. Asp. 568 (2019) 184–194, https://doi.org/10.1016/j.colsurfa.2019.02.022.

[44] M. Yahaya Pudza, Z. Zainal Abidin, S. Abdul Rashid, F. Md Yasin, A.S.M. Noor, M. A. Issa, Sustainable synthesis processes for carbon dots through response surface methodology and artificial neural network, Processes 7 (2019) 704, https://doi.org/10.3390/pr7100704.

[45] X. Ma, Y. Dong, H. Sun, N. Chen, Highly fluorescent carbon dots from peanut shells as potential probes for copper ion: the optimization and analysis of the synthetic process, Mater. Today Chem. 5 (2017) 1–10, https://doi.org/10.1016/j.mtchem.2017.04.004.

[46] Q. Tan, X. Li, P. Sun, J. Zhao, Q. Yang, L. Wang, Y. Deng, G. Shen, Fluorescent carbon dots from water hyacinth as detection sensors for ferric ions: the preparation and optimisation using response surface methodology, Anal. Methods 14 (2022) 3573–3582, https://doi.org/10.1039/D2AY01182D.

[47] A. Gattuso, A. Piscopo, R. Romeo, A. De Bruno, M. Poiana, Recovery of bioactive compounds from calabrian bergamot citrus waste: selection of best Green extraction, Agriculture 13 (2023) 1095, https://doi.org/10.3390/agriculture13051095.

[48] E. Tsiokanos, N. Tsafantakis, A. Termentzi, N. Aligiannis, L.A. Skaltsounis, N. Fokialakis, Phytochemical characteristics of bergamot oranges from the ionian islands of Greece: a multi-analytical approach with emphasis in the distribution of neohesperidose flavanones, Food Chem. 343 (2021) 128400, https://doi.org/10.1016/j.foodchem.2020.128400.

[49] A. Irto, S.G.M. Raccuia, G. Lando, C. De Stefano, K. Arena, T.M.G. Salerno, A. Pettignano, F. Cacciola, L. Mondello, P. Cardiano, Valorization of citrus waste for circular economy: a case study on bergamot pomace as sorbent for Cd2+ removal and source of added value compounds, Microchem. J. 193 (2023) 109183, https://doi.org/10.1016/j.microc.2023.109183.

[50] A.M. Brouwer, Standards for photoluminescence quantum yield measurements in solution (IUPAC Technical Report), Pure Appl. Chem. 83 (2011) 2213–2228, https://doi.org/10.1351/PAC-REP-10-09-31.

[51] R. Leardi, C. Melzi, G. Polotti, CAT (Chemom. Agil. Tool.) (2023).

[52] W. KERN, Cleaning solutions based on hydrogen peroxide for use in silicon semiconductor technology, RCA Rev. 31 (1970) 187–206.

[53] S. Giuffrida, G. Ventimiglia, S. Sortino, Straightforward Green synthesis of "naked" aqueous silver nanoparticles, Chem. Commun. (2009) 4055–4057, https://doi.org/10.1039/B907075C.

[54] I. Ielo, F. De Gaetano, E. Piperopoulos, G. De Luca, S. Conoci, Easy One-Pot decoration of graphene oxide nanosheets by Green silver nanoparticles, Int. J. Mol. Sci. 26 (2025) 713, https://doi.org/10.3390/ijms26020713.

[55] D.E. Koppel, Analysis of macromolecular polydispersity in intensity correlation spectroscopy: the method of cumulants, J. Chem. Phys. 57 (1972) 4814–4820, https://doi.org/10.1063/1.1678153.

[56] L. Cui, H.J. Butler, P.L. Martin-Hirsch, F.L. Martin, Aluminium foil as a potential substrate for ATR-FTIR, transflection FTIR or Raman spectrochemical analysis of biological specimens, Anal. Methods 8 (2016) 481–487, https://doi.org/10.1039/C5AY02638E.

[57] C.De Stefano, S. Sammartano, P. Mineo, C. Rigano, Computer tools for the speciation of natural fluids, in: Computer Tools for the Speciation of Natural Fluids, AMSTERDAM, 1997. ⟨https://iris.unime.it/handle/11570/1888699⟩ (accessed February 12, 2025).

[58] J. Yu, N. Song, Y.-K. Zhang, S.-X. Zhong, A.-J. Wang, J. Chen, Green preparation of carbon dots by jinhua bergamot for sensitive and selective fluorescent detection of Hg2+ and Fe3+, Sens. Actuators B Chem. 214 (2015) 29–35, https://doi.org/10.1016/j.snb.2015.03.006.

[59] S. Šafranko, A. Stanković, S. Hajra, H.-J. Kim, I. Strelec, M. Dutour-Sikirić, I. Weber, M.H. Bosnar, P. Grbčić, S.K. Pavelić, A. Széchenyi, Y.K. Mishra, I. Jerković, S. Jokić, Preparation of multifunctional N-Doped carbon quantum dots from citrus clementina peel: investigating targeted pharmacological activities and the potential application for Fe3+ sensing, Pharmaceuticals 14 (2021) 857, https://doi.org/10.3390/ph14090857.

[60] C. Wang, H. Shi, M. Yang, Y. Yan, E. Liu, Z. Ji, J. Fan, Facile synthesis of novel carbon quantum dots from biomass waste for highly sensitive detection of iron ions, Mater. Res. Bull. 124 (2020) 110730, https://doi.org/10.1016/j.materresbull.2019.110730.

[61] A.M. Senol, E. Bozkurt, Facile Green and one-pot synthesis of seville Orange derived carbon dots as a fluorescent sensor for Fe3+ ions, Microchem. J. 159 (2020) 105357, https://doi.org/10.1016/j.microc.2020.105357.

[62] Z. Fatahi, N. Esfandiari, H. Ehtesabi, Z. Bagheri, H. Tavana, Z. Ranjbar, H. Latifi, Physicochemical and cytotoxicity analysis of Green synthesis carbon dots for cell imaging, EXCLI J. 18 (2019) 454–466, https://doi.org/10.17179/excli2019-1465.

[63] J. Zhang, J. Zhang, Y. Shan, C. Guo, L. He, L. Zhang, W. Ling, Y. Liang, B. Zhong, Effect of harvest time on the chemical composition and antioxidant capacity of gannan navel Orange (*citrus sinensis* L. Osbeck 'Newhall') juice, J. Integr. Agric. 21 (2022) 261–272, https://doi.org/10.1016/S2095-3119(20)63395-0.

[64] D. Ozyurt, M.A. Kobaisi, R.K. Hocking, B. Fox, Properties, synthesis, and applications of carbon dots: a review, Carbon Trends 12 (2023) 100276, https://doi.org/10.1016/j.cartre.2023.100276.

[65] G.S. Das, J.P. Shim, A. Bhatnagar, K.M. Tripathi, T. Kim, Biomass-derived carbon quantum dots for Visible-Light-Induced photocatalysis and Label-Free detection of Fe(III) and ascorbic acid, Sci. Rep. 9 (2019) 15084, https://doi.org/10.1038/s41598-019-49266-y.

[66] Q. Xu, Q. Zhou, Z. Hua, Q. Xue, C. Zhang, X. Wang, D. Pan, M. Xiao, Single-Particle spectroscopic measurements of fluorescent graphene quantum dots, ACS Nano 7 (2013) 10654–10661, https://doi.org/10.1021/nn4053342.

[67] A.B. Siddique, S.M. Hossain, A.K. Pramanick, M. Ray, Excitation dependence and independence of photoluminescence in carbon dots and graphene quantum dots: insights into the mechanism of emission, Nanoscale 13 (2021) 16662–16671, https://doi.org/10.1039/D1NR04301C.

[68] A. Sharma, T. Gadly, A. Gupta, A. Ballal, S.K. Ghosh, M. Kumbhakar, Origin of excitation dependent fluorescence in carbon nanodots, J. Phys. Chem. Lett. 7 (2016) 3695–3702, https://doi.org/10.1021/acs.jpclett.6b01791.

[69] K.P. Loh, Q. Bao, G. Eda, M. Chhowalla, Graphene oxide as a chemically tunable platform for optical applications, Nat. Chem. 2 (2010) 1015–1024, https://doi.org/10.1038/nchem.907.

[70] C.C. Zhang, S. Hartlaub, I. Petrovic, B. Yilmaz, Raman spectroscopy characterization of amorphous coke generated in industrial processes, ACS Omega 7 (2022) 2565–2570, https://doi.org/10.1021/acsomega.1c03456.

[71] A. Sadezky, H. Muckenhuber, H. Grothe, R. Niessner, U. Pöschl, Raman microspectroscopy of soot and related carbonaceous materials: spectral analysis and structural information, Carbon 43 (2005) 1731–1742, https://doi.org/10.1016/j.carbon.2005.02.018.

[72] O. Zaca-Moran, F. Díaz-Monge, A. Rodríguez-Juárez, C.L. Gómez-Muñoz, P. Zaca-Moran, O. Secundino-Sánchez, J. Díaz-Reyes, Synthesis and characterization of fluorescent carbon dots obtained from citrus x sinensis by an eco-friendly method, Results Chem. 11 (2024) 101788.

[73] F. Barzegar, A. Bello, D. Momodu, M.J. Madito, J. Dangbegnon, N. Manyala, Preparation and characterization of porous carbon from expanded graphite for high energy density supercapacitor in aqueous electrolyte, J. Power Sources 309 (2016) 245–253, https://doi.org/10.1016/j.jpowsour.2016.01.097.

[74] S. Claramunt, A. Varea, D. López-Díaz, M.M. Velázquez, A. Cornet, A. Cirera, The importance of interbands on the interpretation of the Raman spectrum of graphene oxide, J. Phys. Chem. C. 119 (2015) 10123–10129, https://doi.org/10.1021/acs.jpcc.5b01590.

[75] A.Y. Lee, K. Yang, N.D. Anh, C. Park, S.M. Lee, T.G. Lee, M.S. Jeong, Raman study of D* band in graphene oxide and its correlation with reduction, Appl. Surf. Sci. 536 (2021) 147990, https://doi.org/10.1016/j.apsusc.2020.147990.

[76] K. Kim, S. Coh, L.Z. Tan, W. Regan, J.M. Yuk, E. Chatterjee, M.F. Crommie, M. L. Cohen, S.G. Louie, A. Zettl, Raman spectroscopy study of rotated Double-Layer graphene: Misorientation-Angle dependence of electronic structure, Phys. Rev. Lett. 108 (2012) 246103, https://doi.org/10.1103/PhysRevLett.108.246103.

[77] J. Wu, P. Wang, F. Wang, Y. Fang, Investigation of the microstructures of graphene quantum dots (GQDs) by Surface-Enhanced Raman spectroscopy, Nanomaterials 8 (2018) 864, https://doi.org/10.3390/nano8100864.

[78] B. Gayen, S. Palchoudhury, J. Chowdhury, Carbon dots: a mystic star in the world of nanoscience, J. Nanomater. 2019 (2019) 1–19, https://doi.org/10.1155/2019/3451307.

[79] E. Dervishi, Z. Ji, H. Htoon, M. Sykora, S.K. Doorn, Raman spectroscopy of bottom-up synthesized graphene quantum dots: size and structure dependence, Nanoscale 11 (2019) 16571–16581, https://doi.org/10.1039/C9NR05345J.

[80] F.J. Chao-Mujica, L. Garcia-Hernández, S. Camacho-López, M. Camacho-López, M.A. Camacho-López, D. Reyes Contreras, A. Pérez-Rodríguez, J.P. Peña-Caravaca, A. Páez-Rodríguez, J.G. Darias-Gonzalez, L. Hernandez-Tabares, O. Arias de Fuentes, E. Prokhorov, N. Torres-Figueredo, E. Reguera, L.F. Desdin-García, Carbon quantum dots by submerged arc discharge in water: synthesis, characterization, and mechanism of formation, J. Appl. Phys. 129 (2021), https://doi.org/10.1063/5.0040322.

[81] R. Saincher, S. Kumar, P. Gopalkrishna, M. Maithri, P. Sherigar, Comparison of color accuracy and picture quality of digital SLR, point and shoot and mobile cameras used for dental intraoral photography – a pilot study, Heliyon 8 (2022) e09262, https://doi.org/10.1016/j.heliyon.2022.e09262.

[82] M. Preethi, C. Viswanathan, N. Ponpandian, A metal-free, dual catalyst for the removal of rhodamine b using novel carbon quantum dots from muskmelon peel under sunlight and ultrasonication: a Green way to clean the environment, J. Photochem. Photobiol. A Chem. 426 (2022) 113765, https://doi.org/10.1016/j.jphotochem.2021.113765.

[83] F. Tuinstra, J.L. Koenig, Raman spectra of graphite, J. Chem. Phys. 53 (1970) 1126–1130.

[84] S.G.M. Raccuia, E. Zanda, C. Bretti, M. Formica, E. Macedi, A. Melchior, M. Tolazzi, M. Sanadar, D. Lascari, G. De Luca, A. Irto, C. De Stefano, P. Cardiano, G. Lando, Multi-Analytical approach for the Acid-Base, thermal and surface properties assessment of waste biomasses, Molecules 29 (2024) 5735, https://doi.org/10.3390/molecules29235735.

[85] M. Ullah, U.A. Awan, H. Ali, A. Wahab, S.U. Khan, M. Naeem, M. Ruslin, A. Z. Mustopa, N. Hasan, Carbon dots: new rising stars in the carbon family for diagnosis and biomedical applications, J. Nanotheranostics 6 (1) (2025), https://doi.org/10.3390/jnt6010001.

[86] F. Yuan, S. Li, Z. Fan, X. Meng, L. Fan, S. Yang, Shining carbon dots: synthesis and biomedical and optoelectronic applications, Nano Today 11 (2016) 565–586, https://doi.org/10.1016/j.nantod.2016.08.006.

[87] B.D. Mansuriya, Z. Altintas, Carbon dots: classification, properties, synthesis, characterization, and applications in health Care—An updated review (2018–2021), Nanomaterials 11 (2021) 2525, https://doi.org/10.3390/nano11102525.

[88] Y. Lou, X. Hao, L. Liao, K. Zhang, S. Chen, Z. Li, J. Ou, A. Qin, Z. Li, Recent advances of biomass carbon dots on syntheses, characterization, luminescence mechanism, and sensing applications, Nano Sel. 2 (2021) 1117–1145, https://doi.org/10.1002/nano.202000232.

[89] W.K. Szapoczka, A.L. Truskewycz, T. Skodvin, B. Holst, P.J. Thomas, Fluorescence intensity and fluorescence lifetime measurements of various carbon dots as a function of ph, Sci. Rep. 13 (2023) 10660, https://doi.org/10.1038/s41598-023-37578-z.

[90] M.T. Genc, G. Yanalak, G. Arslan, I.H. Patir, Green preparation of carbon quantum dots using *gingko biloba* to sensitize TiO2 for the photohydrogen production, Mater. Sci. Semicond. Process. 109 (2020) 104945, https://doi.org/10.1016/j.mssp.2020.104945.

[91] D. Rodríguez-Padrón, M. Algarra, L.A.C. Tarelho, J. Frade, A. Franco, G. de Miguel, J. Jiménez, E. Rodríguez-Castellón, R. Luque, Catalyzed Microwave-Assisted preparation of carbon quantum dots from lignocellulosic residues, ACS Sustain. Chem. Eng. 6 (2018) 7200–7205, https://doi.org/10.1021/acssuschemeng.7b03848.

[92] P. Luo, Y. Yu, X. Guan, Preparation of carbon nitride dots with sizes larger than 20 nm, Appl. Sci. 9 (2019) 464, https://doi.org/10.3390/app9030464.

[93] R. Liu, D. Wu, X. Feng, K. Müllen, Bottom-Up fabrication of photoluminescent graphene quantum dots with uniform morphology, J. Am. Chem. Soc. 133 (2011) 15221–15223, https://doi.org/10.1021/ja204953k.

[94] S. Ahmadian-Fard-Fini, M. Salavati-Niasari, D. Ghanbari, Hydrothermal Green synthesis of magnetic Fe3O4-carbon dots by lemon and grape fruit extracts and as a photoluminescence sensor for detecting of *e. coli* bacteria, Spectrochim. Acta Part A Mol. Biomol. Spectrosc. 203 (2018) 481–493, https://doi.org/10.1016/j.saa.2018.06.021.

[95] H. Yu, X. Li, X. Zeng, Y. Lu, Preparation of carbon dots by non-focusing pulsed laser irradiation in toluene, Chem. Commun. 52 (2015) 819–822, https://doi.org/10.1039/C5CC08384B.

[96] R. Kumar, V.B. Kumar, A. Gedanken, Sonochemical synthesis of carbon dots, mechanism, effect of parameters, and catalytic, energy, biomedical and tissue engineering applications, Ultrason. Sonochem. 64 (2020) 105009, https://doi.org/10.1016/j.ultsonch.2020.105009.

[97] S. Zhuo, M. Shao, S.-T. Lee, Upconversion and downconversion fluorescent graphene quantum dots: ultrasonic preparation and photocatalysis, ACS Nano 6 (2012) 1059–1064, https://doi.org/10.1021/nn2040395.

[98] A. Liscio, K. Kouroupis-Agalou, X.D. Betriu, A. Kovtun, E. Treossi, N.M. Pugno, G. De Luca, L. Giorgini, V. Palermo, Evolution of the size and shape of 2D nanosheets during ultrasonic fragmentation, 2D Mater. 4 (2017) 025017, https://doi.org/10.1088/2053-1583/aa57ff.

[99] S.K. Filippov, R. Khusnutdinov, A. Murmiliuk, W. Inam, L.Y. Zakharova, H. Zhang, V.V. Khutoryanskiy, Dynamic light scattering and transmission electron microscopy in drug delivery: a roadmap for correct characterization of nanoparticles and interpretation of results, Mater. Horiz. 10 (2023) 5354–5370, https://doi.org/10.1039/D3MH00717K.

[100] C.N. Lunardi, A.J. Gomes, F.S. Rocha, J. De Tommaso, G.S. Patience, Experimental methods in chemical engineering: zeta potential, Can. J. Chem. Eng. 99 (2021) 627–639, https://doi.org/10.1002/cjce.23914.

[101] S. Zhu, Y. Song, J. Wang, H. Wan, Y. Zhang, Y. Ning, B. Yang, Photoluminescence mechanism in graphene quantum dots: quantum confinement effect and surface/edge state, Nano Today 13 (2017) 10–14, https://doi.org/10.1016/j.nantod.2016.12.006.

[102] A. Bhattacharya, S. Chatterjee, R. Prajapati, T.K. Mukherjee, Size-dependent penetration of carbon dots inside the ferritin nanocages: evidence for the quantum confinement effect in carbon dots, Phys. Chem. Chem. Phys. 17 (2015) 12833–12840, https://doi.org/10.1039/C5CP00543D.

[103] F. de Andrés, Á. Ríos, Carbon dots – separative techniques: tools-objective towards Green analytical nanometrology focused on bioanalysis, Microchem. J. 161 (2021) 105773, https://doi.org/10.1016/j.microc.2020.105773.

[104] N. Ullal, R. Mehta, D. Sunil, Separation and purification of fluorescent carbon dots – an unmet challenge, Analyst 149 (2024) 1680–1700, https://doi.org/10.1039/D3AN02134C.

[105] V. Michaud, J. Pracht, F. Schilfarth, C. Damm, B. Platzer, P. Haines, C. Harreiß, D. M. Guldi, E. Spiecker, W. Peukert, Well-separated water-soluble carbon dots via gradient chromatography, Nanoscale 13 (2021) 13116–13128, https://doi.org/10.1039/D1NR02562G.

[106] J.C. Vinci, L.A. Colón, Surface chemical composition of chromatographically fractionated graphite nanofiber-derived carbon dots, Microchem. J. 110 (2013) 660–664, https://doi.org/10.1016/j.microc.2013.08.002.

[107] P. Zuo, X. Lu, Z. Sun, Y. Guo, H. He, A review on syntheses, properties, characterization and bioanalytical applications of fluorescent carbon dots, Microchim Acta 183 (2016) 519–542, https://doi.org/10.1007/s00604-015-1705-3.

[108] V. Ţucureanu, A. Matei, A.M. Avram, FTIR spectroscopy for carbon family study, Crit. Rev. Anal. Chem. 46 (2016) 502–520, https://doi.org/10.1080/10408347.2016.1157013.

[109] O. Zaca-Moran, F. Díaz-Monge, A. Rodríguez-Juárez, C.L. Gómez-Muñoz, P. Zaca-Moran, O. Secundino-Sánchez, J. Díaz-Reyes, Synthesis and characterization of fluorescent carbon dots obtained from *citrus x sinensis* by an eco-friendly method, Results Chem. 11 (2024) 101788, https://doi.org/10.1016/j.rechem.2024.101788.

[110] A. Kundu, S. Basu, B. Maity, Upcycling waste: citrus limon peel-derived carbon quantum dots for sensitive detection of tetracycline in the nanomolar range, ACS Omega 8 (2023) 36449–36459, https://doi.org/10.1021/acsomega.3c05424.

[111] M.J. Deka, P. Dutta, S. Sarma, O.K. Medhi, N.C. Talukdar, D. Chowdhury, Carbon dots derived from water hyacinth and their application as a sensor for pretilachlor, Heliyon 5 (2019) e01985, https://doi.org/10.1016/j.heliyon.2019.e01985.

[112] I. Alkian, H. Sutanto, Hadiyanto, Quantum yield optimization of carbon dots using response surface methodology and its application as control of Fe3+ion levels in drinking water, Mater. Res. Express 9 (2022) 015702, https://doi.org/10.1088/2053-1591/ac3f60.

[113] L. Zhao, Y. Wang, X. Zhao, Y. Deng, Y. Xia, Facile synthesis of nitrogen-doped carbon quantum dots with chitosan for fluorescent detection of Fe3+, Polymers 11 (2019) 1731, https://doi.org/10.3390/polym11111731.

[114] A. Dager, T. Uchida, T. Maekawa, M. Tachibana, Synthesis and characterization of Mono-disperse carbon quantum dots from fennel seeds: photoluminescence analysis using machine learning, Sci. Rep. 9 (2019) 14004, https://doi.org/10.1038/s41598-019-50397-5.

[115] J. Bonet, M. Filella, P.M. May, R.F. May, K. MurrayJESS Thermodynamic database of chemical reactions v8.9, (2023). https://doi.org/10.5281/zenodo.7700024.

[116] J. Singh, S. Kaur, J. Lee, A. Mehta, S. Kumar, K.-H. Kim, S. Basu, M. Rawat, Highly fluorescent carbon dots derived from *mangifera indica* leaves for selective detection of metal ions, Sci. Total Environ. 720 (2020) 137604, https://doi.org/10.1016/j.scitotenv.2020.137604.

[117] T.C. Araújo, H. dos S. Oliveira, J.J.S. Teles, J.D. Fabris, L.C.A. Oliveira, J.P. de Mesquita, Hybrid heterostructures based on hematite and highly hydrophilic carbon dots with photocatalytic activity, Appl. Catal. B Environ. 182 (2016) 204–212, https://doi.org/10.1016/j.apcatb.2015.09.036.

[118] L.A. Alves, A.H. de Castro, F.G. de Mendonça, J.P. de Mesquita, Characterization of acid functional groups of carbon dots by nonlinear regression data fitting of potentiometric titration curves, Appl. Surf. Sci. 370 (2016) 486–495, https://doi.org/10.1016/j.apsusc.2016.02.128.

[119] Z.L. Wu, M.X. Gao, T.T. Wang, X.Y. Wan, L.L. Zheng, C.Z. Huang, A general quantitative ph sensor developed with dicyandiamide N-doped high quantum yield graphene quantum dots, Nanoscale 6 (2014) 3868–3874, https://doi.org/10.1039/C3NR06353D.